Delft University of Technology
Department of Materials Science and Engineering

Effect of microstructure on the degradation of 3D printed Mg-4Zn porous scaffolds

A thesis submitted to the Faculty of 3mE for the degree of Master of Science in Materials Science and Engineering.

Author
W.Y. Kong BSc.

Supervisors
Dr. Y. Gonzalez-Garcia
Dr. J. Zhou
J. Dong MSc.

October 21, 2021

Abstract

Many manufacturing industries have been impacted by the innovation of additive manufacturing (AM), and biomaterials manufacturing is no exception. One group of biomaterials impacted by the innovation of 3D printing are degradable biomaterials. Degradable biomaterials could eliminate the need for surgery to remove the implant. 3D printed porous degradable biomaterials provide both mechanical support and space for bone ingrowth. As of today, there is an absence of materials for this application that are biodegradable, biocompatible and can be 3D printed. Magnesium can be used as a degradable biomaterial but its corrosion resistance is not yet adequate for application in the human body. Applying zinc as an alloying element to magnesium increases its corrosion resistance compared to pure magnesium. As the addition of alloying elements changes the microstructure, which in turn changes its corrosion behaviour.

This thesis analysed the effect of microstructure on the corrosion behaviour of extrusion-based 3D printed porous Mg-4Zn (wt.%) scaffolds, using localised electrochemical techniques i.e. scanning Kelvin probe force microscopy (SKPFM) and scanning electrochemical microscopy (SECM). The microstructure of the Mg-4Zn scaffolds includes grains with secondary phases precipitated along the grain boundaries with the presence of micropores. The secondary phase particles showed increased Volta-potential compared to the magnesium-based matrix. Therefore, the addition of zinc caused micro-galvanic coupling between secondary phase particles and the matrix, but their contribution to corrosion is minimal due to postponed contact with the electrolyte and the protection by the corrosion products. Micropores in the Mg-4Zn scaffold increased the surface exposed to fluids and were pitting corrosion initiation sites. During corrosion however, the surface was covered with a more stable corrosion product compared to pure magnesium. As a result of this, the corrosion resistance of Mg-4Zn scaffolds is better than pure magnesium scaffolds.

Contents

List of Figures

List of Tables

Chapter 1

Introduction

This chapter serves as an introduction to the main topics discussed in the thesis. The background information is considered essential to understanding the results of the thesis. This includes the selection of materials, the corrosion mechanism of magnesium, the fabrication method and its effect on the microstructure will also be explained. Finally, local corrosion and the electrochemical techniques used to investigate the effect of microstructure on the corrosion will be discussed.

3D printing, commonly referred to as additive manufacturing (AM), is considered to be one of the main global industrial and technological revolutions. 3D printing is defined as a layer-by-layer manufacturing technique used to fabricate three-dimensional products. In recent years, 3D printing has made a significant impact on the manufacturing market. It has the ability to produce complex structures in a fast and reproducible manner, in addition to the advantage of flexibility for specific geometries. Such as hollow or porous structures. Hollow structures reduce the density of the product and the number of raw materials used. Many manufacturing industries have been impacted by the innovation of 3D printing, and biomaterials manufacturing is no exception [1]. 3D printing is considered an ideal method for the fabrication of biomaterials because it can be used to reduce the technical difficulty and the cost of customised production [2]. Biomaterials are defined as *"a substance that has been engineered to take a form which, alone or as part of a complex system, is used to direct, by control of interactions with components of living systems, the course of any therapeutic or diagnostic procedure, in human or veterinary medicine"* [3]. One possible application of biomaterials are scaffolds for bones, which are the structures engineered to allow desirable interactions for the formation of new tissue and bones.

Bones have multiple functions; they provide structural support, protection for vital organs, mechanical support for soft tissues and they play a role in the storing of minerals. The design and fabrication of complex porous scaffolds to mimic the structure and properties of natural bone is a major challenge in the field of tissue engineering. Tissue engineering applies the principles of engineering and life sciences for the development of biological scaffolds to improve tissue or organ functions such as regenerative properties [4]. Bones are self-healing under normal circumstances. However, after trauma, disease or ageing, the regenerative property can become weaker and thus may need help.

Natural bone is a porous composite material, consisting mainly of hydroxyapatite crystals (2 entities of $Ca_5(PO_4)_3(OH)$, also denoted as $Ca_{10}(PO_4)_6(OH)_2$). Hydroxyapatite is a mineral

form of calcium apatite which lays in an organic matrix of collagen [5]. Bone consists of porous cancellous (trabecular) bone surrounded by the less porous compact (cortical) bone. The pore size of cancellous bone ranges from 200 µm to 1000 µm and its porosity, defined as the percentage of void space in a solid structure, ranges from 40% to 95%. The porosity of compact bone ranges from 5% to 20% [6]. Pores are easily incorporated into structures when the implants are manufactured using 3D printing. The porosity of metallic scaffolds can be made to be similar to the level of porosity found in the natural bones. An advantage of incorporating pores in metallic implants is the reduction of the elastic modulus of the metal, providing space for bone in-growth, body fluid circulation and support for cell proliferation [7].

When gaps in bones are greater than 30 mm it cannot fully heal on its own [8]. Scaffolds help the healing but the question that arises is, what materials can be used to provide support for bone healing. Permanent scaffolds from biocompatible metals have high mechanical strength, often too high compared to bone. This strength will induce stress shielding and causes bone resorption [9]. Biocompatibility refers to the ability to perform without eliciting undesirable effects in the recipient and generating the most appropriate beneficial cellular or tissue response [10]. Bone scaffolds manufactured from materials such as polymers have shown good biocompatibility, biodegradability and promote bone growth, although there are concerns with the inflammatory responses and resorption of the by-product [11]. For orthopaedic implants, metals and alloys are widely used for their biocompatibility, mechanical strength and wear resistance.

Porous biomaterials have been made from bio-inert materials such as titanium, stainless steel, tantalum, nitinol or cobalt-chromium alloys. These materials are limited by the necessity of a removal surgery. Since, when they are left in the body for a prolonged time, they could release toxic ions resulting in cell death and breakdown of bone substances [12]. degradable biomaterials could solve the above-mentioned limitations of existing scaffolds since they do not require removal nor do they disturb bone regeneration. Porous scaffolds have even been found to accelerate bone regeneration when the scaffolds were biofunctionalised to release antibacterial and osteogenic agents [13].

1.1 Biodegradable materials for porous scaffolds

However, 3D printed porous scaffolds are not yet suitable for application in the body. The main issue is a lack of materials that can be used for 3D printing, in addition to being degradable and biocompatible. Currently, no material has been found that holds all three of these properties. A brief analysis of a few materials can help explain this. Beginning with iron. Iron exhibits too slow degradation. Large portions of pure iron stents remained intact in the blood vessels after twelve months, which caused reactions similar to those found with the application of permanent scaffolds [2]. Another limitation is that iron shows ferromagnetism. This negatively impacts the compatibility with imaging devices, such as magnetic resonance imaging (MRI). A way around the latter limitation might be to use a material like magnesium, as this does not show ferromagnetism. However, where iron showed too low degradation rates, magnesium shows too high degradation rates. Though, magnesium-based alloys have been investigated and showed promising results for the application of biodegradable porous scaffolds.

These promising results require a bit more elucidation. Magnesium possesses excellent biocompatibility and preferable mechanical properties; magnesium alloys have a specific density (1.74–2 g/cm^3) and Young's modulus (41–45 GPa), which are similar to human bones (1.8–2.1 g/cm^3 and 3–20 GPa respectively) [14]. The low Young's modulus of magnesium prevents the mechanical failure of surrounding bone due to stress shielding. Magnesium biomaterials conserve their mechanical strength well in the early stages but pure magnesium scaffolds corrode too fast to keep

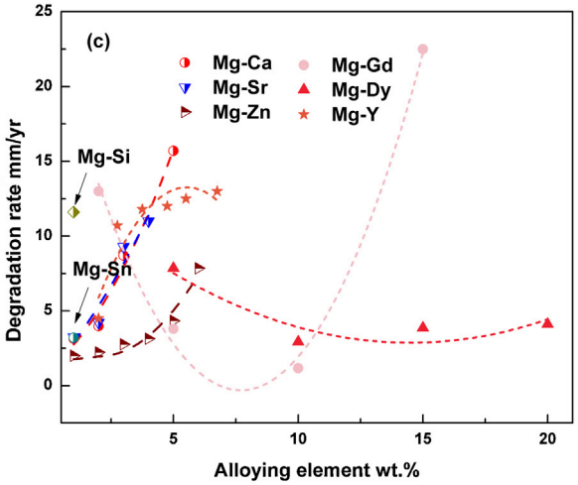

Figure 1.1: Degradation rates for binary Mg–X alloys as a function of alloying element content [17].

their integrity for their load-bearing function. Therefore, the corrosion rate of pure magnesium should be decreased.

To decrease the corrosion rate of magnesium, alloying elements, such as calcium, strontium, zinc and rare-earth elements are used in non-medical applications. However, for use in the medical field, the alloying elements should be biocompatible; i.e. they should not release toxic elements during degradation. Furthermore, they also need to influence the corrosion behaviour of magnesium in a beneficial way when added in precise amounts. Figure 1.1 shows the effect of calcium, strontium, zinc, gadolinium, dysprosium and yttrium as alloying elements on the corrosion of magnesium. The figure shows that the addition of these elements to magnesium influences its degradation rate differently.

Most magnesium alloys for biomedical applications include aluminium or rare earth metals. However, aluminium is not suitable for degradable implants as it is harmful to neurons, osteoblast and aluminium is associated with dementia and Alzheimer's disease [15, 16]. Yttrium and seventeen other rare earth metals were considered suitable for biodegradable magnesium alloys [17]. The rare earth elements improve high-temperature strength and creep resistance for magnesium. The degradation rate of binary magnesium alloys with yttrium, gadolinium and dysprosium all depends on each element's concentration. The optimal amounts were 2 wt.% for yttrium, 10 wt.% for dysprosium and 15 wt.% for gadolinium [18–20]. Long term exposure to yttrium ions however has been shown to change the expression of genes and shown adverse effects on DNA transcription factors in rats [21]. Rare earth metals are unsuitable alloying elements for biodegradable magnesium alloys when they are above certain levels. Therefore, there is still a demand for the development of magnesium alloys without aluminium or rare earth metals.

Other candidates as alloying elements in magnesium include calcium, strontium, manganese, zirconium, silicon, tin and zinc [17]. Calcium and strontium share similar chemical and metallurgical properties as they both belong to group 2 of the periodic table. The incorporation of the two elements into magnesium leads to the precipitation of secondary phases is (Mg_2Ca and $Mg_{17}Sr_2$) along the grain boundaries. These secondary intermetallic phases are thermally stable, which improves the strength and creep properties. Calcium and strontium can also refine the microstructure of magnesium and in that way improve the strength and creep properties. But these intermetallic phases are brittle and brittle phases in magnesium act as potential sources for cracking. The intermetallic secondary phases also accelerate the degradation due to galvanic

corrosion. The solubility of calcium and strontium in magnesium is relatively limited; about 1.34 wt.% and 0.11 wt.% respectively under equilibrium conditions, limiting the advantageous effects on magnesium [17]. Therefore, calcium and strontium cannot be used on their own as alloying elements, rather they can be used to enhance mechanical and degradation properties of biodegradable magnesium-based biomaterials.

Silicon is the most effective alloying element to improve the strength due to the precipitation of the Mg_2Si secondary phase. But the secondary phase accelerates the degradation rate. Zirconium decreases the degradation of magnesium when the alloying amount of zirconium in magnesium is less than 1 wt%. When the amount was increased from 1 to 5 wt.%, the degradation became worse [22]. Zirconium is used as a refiner for magnesium alloys.

Zinc is one of the most abundant elements in the human body and is safe for biomedical applications in scaffolds. In addition, zinc has strengthening effects in magnesium, is beneficial for increasing impurities tolerance limits and zinc can improve the castability of magnesium as an alloying element [23]. There are five intermetallic phases between magnesium and zinc; Mg_7Zn_3, MgZn, Mg_2Zn_3, $MgZn_2$ and Mg_2Zn_{11} [24]. With the addition of alloying elements comes a change in microstructure and thus its effect on corrosion. It has been shown that the addition of 4 wt.% of zinc to magnesium decreases the corrosion rate of 3D printed implants. But there is still an essential lack of understanding of the influence of microstructural features on the corrosion of 3D printed implants. Insight into the microstructure-corrosion relation is needed to accomplish proper corrosion rate in magnesium scaffolds.

Pure magnesium corrodes too fast for applications as porous scaffolds, resulting in high amounts of hydrogen generation and local pH increase. Therefore, the corrosion rate needs to be decreased. In the past, the focus had been on microstructure-strength relations, which is important for load-bearing applications, however, there is a lack of knowledge of microstructure-corrosion relations. To understand the corrosion mechanism of Mg-4Zn scaffolds, the degradation of pure magnesium needs to be discussed first. In addition, the change in microstructural features and the effect of microstructural features on this degradation needs to be analysed. This will be the topic of the next two sections.

1.2 Degradation of magnesium

Degradation is caused by the corrosion of metallic materials. General corrosion, pitting corrosion and localised corrosion are the most common encountered corrosion mechanisms of magnesium alloys in simulated physiological fluids [25]. The degradation of magnesium alloys in the body adopt generalised corrosion mechanisms; anodic dissolution of metal and a reduction reaction resulting in oxides, hydroxides, hydrogen gas and other compounds. Magnesium is less stable than zinc in the body and loses electrons when contact is made with water to facilitate hydrogen evolution. Therefore, the corrosion of magnesium is the main event driving the degradation of Mg-Zn alloys. The corrosion mechanism occurs as follows [26].

Anodic dissolution :

$$\mathrm{Mg} \longrightarrow \mathrm{Mg^{2+}} + 2\,\mathrm{e^-} \tag{1.1}$$

Cathodic process :

$$2\,\mathrm{H_2O} + 2\,\mathrm{e^-} \longrightarrow 2\,\mathrm{OH^-} + \mathrm{H_2} \tag{1.2}$$

Alternatively, hydroxide can also be formed, when oxygen reacts water to form hydroxide ions [27]:

$$\mathrm{O_2} + 2\,\mathrm{H_2O} + 4\,\mathrm{e^-} \longrightarrow 4\,\mathrm{OH^-} \tag{1.3}$$

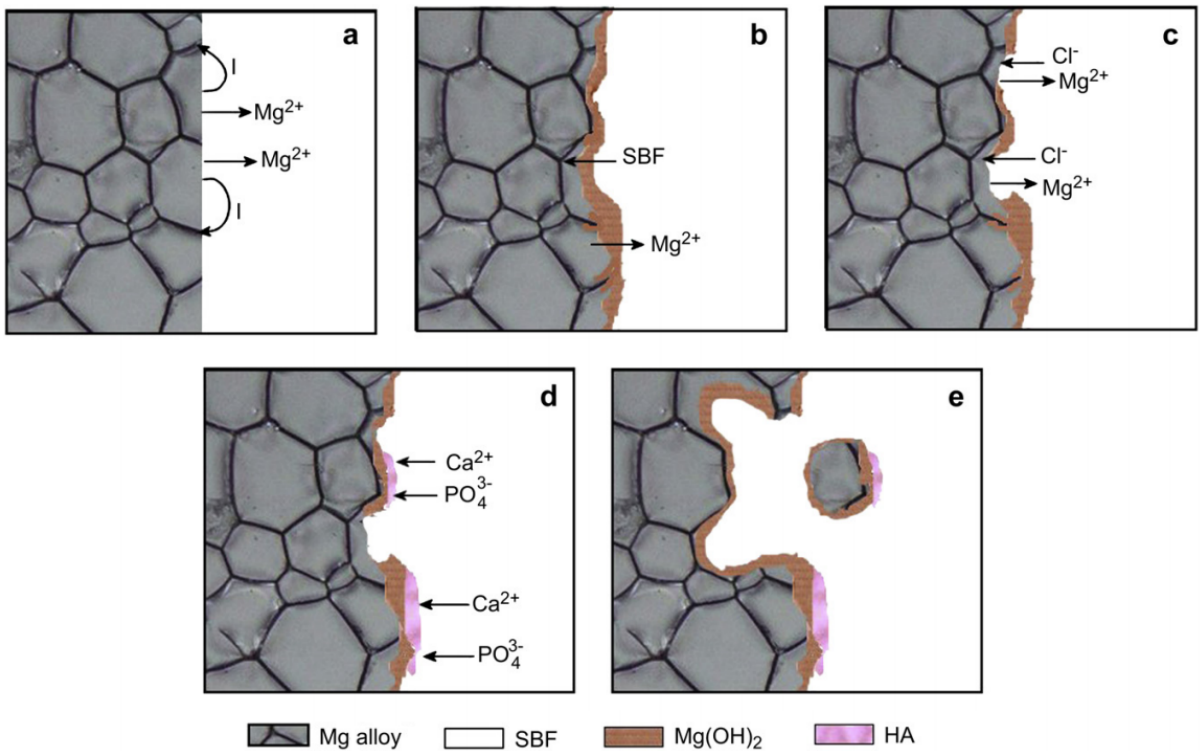

Figure 1.2: Corrosion mechanism of magnesium-based alloy and the formation of hydroxyapatite in simulated body fluid (SBF). (a) Anodic dissolution and reduction reaction; (b) hydroxide layer formation; (c) pit formation; (d) calcium/phosphorus layer formation; (e) release of small particles [26].

Magnesium ions react with the hydroxide to form a protecting magnesium hydroxide ($Mg(OH)_2$) film on the surface

$$Mg^{2+} + 2\,OH^- \longrightarrow Mg(OH)_2 \tag{1.4}$$

The total reaction can be summarised by:

$$Mg + 2\,H_2O \longrightarrow Mg(OH)_2 + H_2 \tag{1.5}$$

The magnesium hydroxide film on the surface will protect the underlying magnesium from contact with body fluids. But the magnesium hydroxide layer is porous and therefore its protection capacity is low. The fluids can penetrate through the pores of the magnesium hydroxide film and react with the magnesium, which leads the chemical reaction inward, while the magnesium ions diffuse outward to form a thicker magnesium hydroxide film on the surface. The formation of the magnesium hydroxide film can be seen in Figure 1.2 a and b. The presence of chloride ions in the body disrupts the homeostasis of dissolution and precipitation processes of the protecting magnesium hydroxide, see Figure 1.2c. Chloride ions react with magnesium hydroxide or react directly with magnesium into more soluble magnesium chloride ($MgCl_2$) as follows [28].

$$Mg(OH)_2 + 2\,Cl^- \longrightarrow MgCl_2 + 2\,OH^- \tag{1.6}$$

$$Mg + 2\,Cl^- \longrightarrow MgCl_2 \tag{1.7}$$

The reaction of magnesium hydroxide into magnesium chloride increases the surface activity due to the decreasing solid protecting magnesium hydroxide. The area is less protected and further dissolution of magnesium is stimulated [28].

In addition to general corrosion, pitting corrosion is accelerated in magnesium as a consequence of the chloride attack and naturally occurs in magnesium [29]. Pitting corrosion results in the release of irregularly shaped particles from the scaffold, promoting the further breakdown of the scaffold (Figure 1.2 e). These magnesium particles do not pose a treat to the human body, as the particles can be disintegrated in the microenvironment of macrophages [26]. A great advantage of magnesium is that the degraded magnesium can be efficiently secreted through the urinary system [14, 30].

As magnesium degrades, hydroxyapatite and other calcium-phosphorous compounds are favoured to form on magnesium hydroxide film. The local pH increases due to the ongoing hydrogen reaction and stimulates hydroxyapatite nucleation. Calcium and phosphate ions get consumed to allow for hydroxyapatite nucleation and growth. The calcium and phosphorous compounds originate from the blood plasma.

$$H_2PO_4 + 2\,OH^- \longrightarrow {PO_4}^{3-} + 2\,H_2O \tag{1.8}$$

$$5\,{Ca}^{2+} + 3\,{PO_4}^{3-} + OH^- \longrightarrow Ca_5(PO_4)_3(OH) \tag{1.9}$$

As mentioned before, the corrosion rate of pure magnesium is too high for it to be used as porous scaffolds. Therefore alloying elements are essential to increase the corrosion resistance of magnesium. Having discussed the degradation mechanism of pure magnesium, attention is now given to the effects of alloying elements on the microstructure of magnesium. As well as a brief discussion about the effects of AM techniques on the microstructure.

1.3 Microstructure of magnesium alloys using material extrusion-based 3D printing

The 3D printing of porous degradable biomaterials allows for flexibility in the internal and external architecture of orthopaedic implants [31]. This flexibility is advantageous as geometrical and topological characteristics can be tuned to improve bone mimicking properties. These properties include similar porosity to bones and comparable strength. Various AM techniques are developed, each more suitable for certain applications or materials than others. The manufacturing techniques are important to the outcome because the (micro)structure affects the stability of the product.

AM techniques for metallic parts are generally classified into five categories: powder bed fusion, direct energy deposition, binder jetting, sheet lamination and material extrusion [7]. For complex structures such as porous metallic scaffolds, only a few techniques are applicable. Powder bed fusion techniques (selective laser melting (SLM) and selective electron beam melting (SEBM)) are capable of fabricating complex topological structures and therefore dominate the literature [32]. But, material extrusion-based techniques for the production of porous scaffolds are promising, since handling steps of brushing off the loose powder and reusing multi-materials are saved. Another advantage of using extrusion-based 3D printing is the elimination of undesirable compositional changes due to magnesium evaporation and severe oxidation of raw materials because of the high temperatures used. For the microstructure of extrusion-based 3D printed products, there is an absence of residual stresses, cracks, distortions or metallurgical defects which are generally found in SLMed metallic parts [33]. Other possible microstructural features found in SLMed metallic parts are parallel oriented basal planes with respect to the extrusion direction, very fine dendritic structure inside each particle and interdendritic network of secondary (metastable) phases containing increased amounts of alloying elements [34]. Instead, the microstructure of material extrusion-based 3D printed parts is more straightforward as it includes

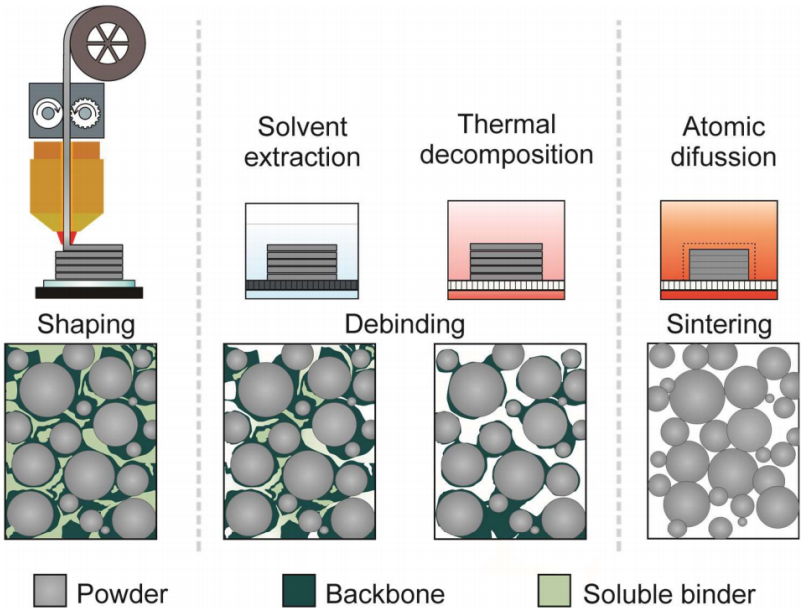

Figure 1.3: Schematic representation of three phases during material extrusion additive manufacturing: shaping, de-binding and sintering [36].

only the incorporation of micropores and the precipitation of secondary phases when alloys are printed.

Material extrusion is a 3D printing technique mostly used for the production of porous polymeric scaffolds, but can also be used for the production of porous metallic scaffolds. The production of porous metallic structures using material extrusion-based 3D printing follows three main steps, shown in Figure 1.3. The first step is shaping, where polymers are mixed with metal powder, the mixture is liquefied above the melting temperature of the polymer, pushed through a nozzle and printed following a predefined path. The extrusion head moves up or the build platform moves down to accommodate the following layer. The material bonds to itself or a secondary build material to form a solid structure as it solidifies [35]. The second step is the de-binding of the polymer. In this step, the polymer is removed by using a solvent, a catalyst or by inducing thermal decomposition. Micropores are found between metal powder particles within a strut which are formed during the removal of the binder. These micropores are interconnected. The last step is sintering, during which loose metal particles coalesce by heating.

The main limitation of material extrusion-based 3D printing is the printing resolution, which is dependent on the particle sizes and nozzle diameter [33]. This nozzle diameter influences the width of the struts, but the strut size should be at least 200 µm to allow bone tissue regeneration. The distance between the struts are called macropores and are obtained by printing the struts in a lay-down pattern of 0°/90° or 0°/60°/120°. The macropores should be between 50 and 800 µm to allow bone tissue regeneration and the porosity of metallic biomaterials should be at least 50% [37]. Taking this into account, the design of porous biomaterials should be tailored for an optimum between the mechanical properties the porous structure needed for bone ingrowth. The macro- and micropores increase the relative surface area to a solution and therefore increase the degradation rate, compared to the bulk alloy. In addition, magnesium is known to corrode rapidly, and it is for this reason that 3D printed pure magnesium scaffolds cannot find their applications in the body. The use of alloying elements, such as zinc, is therefore essential. The addition of zinc imposes a change in microstructure such as precipitation of secondary phases and thus affects the corrosion rate, which will be described in the next subsection.

1.3.1 Secondary phases

Galvanic corrosion is an electrochemical process, which occurs when two metals or alloys are in contact with the presence of an electrolyte. The less noble material will act as an anode and corrode preferentially. The nobility of materials are classified in the galvanic series, where the highest nobility is the most stable and the lowest nobility is the most active. Magnesium is the material with the lowest nobility and thus it will experience an accelerated attack when contact is made with another material in the galvanic series in the presence of an electrolyte. This leads to the anodic metal corroding more quickly than it would without contact and inhibition of the corrosion at the cathode. In addition to galvanic coupling between two dissimilar materials, the galvanic coupling can also occur between the metal and its primary constituents. These constituents include different phases in the material, but impurities can also cause this coupling. The corrosion between the bulk material and primary constituents caused by micro-galvanic coupling is called micro-galvanic corrosion.

Alloying elements could adjust the microstructure by precipitating or changing the microstructure of precipitated phases. Zinc is not entirely soluble in magnesium without extra heat treatments. The insoluble zinc precipitates as a secondary phase frequently called the β-phase. The effect of secondary phases on corrosion is dependent on the distribution; very fine homogeneously distributed secondary phase particles can retard corrosion development [38], while isolated coarse secondary phase particles cause micro-galvanic corrosion [39]. For Mg-3Zn scaffolds this holds; the corrosion resistance increases when the secondary phase particles are distributed homogeneously [40]. Not only the distribution but also the volume fraction of the secondary phase influences the corrosion properties; a higher volume fraction of the second phase results in the worsening of the resistance. It was found that the corrosion resistance decreases as the zinc content increases from 2 to 5 [41] and from 6 to 40.3 wt.% [39]. With increasing zinc content, the amount and area of the secondary phase increases. The secondary phase acted as galvanic cathodes, where the initial hydrogen evolution is stimulated, causing galvanic corrosion acceleration. In extruded Mg-6Zn (wt%) by powder metallurgy, large-size intermetallics of tenths of microns were found. The extruded alloy showed fine equiaxed grains and row elongated grains resulted from partial dynamic recrystallization during hot extrusion. Yan *et al.* revealed that with increasing zinc concentration (6 to 40.3 wt%) the corrosion potential became less negative but the corrosion current increased because of severe micro-galvanic effect, which was caused by more large-size intermetallics [39].

The corrosion resistance increases when the secondary phase particles are homogeneously distributed. However, secondary phase particles are usually not homogeneously distributed throughout the matrix. The grain boundaries are preferred sites for precipitation and segregation in alloys [42]. The addition of zinc also refines the grain size of magnesium-zinc (Mg-Zn) alloys [43]. Grain boundaries in magnesium alloys usually suffer from intergranular corrosion (IGC), which is a localised attack on the grain boundaries [44]. Thus secondary phase particles can further increase the degradation of magnesium from the grain boundaries. This effect of secondary phase particles in IGC becomes clear when the secondary phase is dissolved in the matrix using T4 heat treatment. T4 heat treatment includes heating the Mg-Zn alloy to 450 °C for 2 hours followed by quenching the alloy in water at room temperature. After T4 heat treatment, there are no secondary phases and the corrosion resistance of Mg-5Zn increases [40]. This may be due to its size effect, when a cathode is smaller than the anode, there is a massive attack on the anode, but when the anode is smaller than the cathode, the attack is less severe.

Zinc has been shown to elevate the corrosion potential of Mg-6Zn thus slowing down the *in vitro* degradation rate of the Mg–6Zn alloy compared to high-purity magnesium in simulated body fluid (SBF). A protective layer of hydroxyapatite and other magnesium and calcium phosphates

were formed on the surface when immersed in SBF [45]. Another effect of alloying elements on the corrosion resistance is the effect of the layer of corrosion product. It was stated before that magnesium hydroxide forms on the surface of pure magnesium, which is easily dissolved by chloride ions, but the addition of alloying elements could result in a more stable corrosion layer. It was found that corrosion layers on Mg–6Zn contained zinc after *in vivo* immersion, which could lead to a more stable layer of corrosion products as magnesium hydroxide is porous and its protective capacity is reduced by chloride.

1.3.2 Micropores

The interconnected micropore network increases the area to volume ratio that is exposed to body fluids, compared to bulk Mg-Zn alloys. The increased area makes the scaffold more susceptible to corrosion. Geenen *et al.* [46] fabricated stainless steel parts with SLM and showed that the micropores (around 40 μm in diameter) are preferential sites for corrosion in chloride solutions. The preferential corrosion in micropores is due to a different environment inside the pores, leading to de-passivation of the surface. The type of micropore affects the degradation as well: irregularly shaped pores corrode more easily due to the enrichment of aggressive ions in the corners [47]. Similar events of localised corrosion in porous stainless steel might occur in magnesium; micropores become traps for electrolytes and a chloride-rich local environment is created which can facilitate pitting or crevice corrosion. Crevice corrosion is defined as localised corrosion within narrow gaps formed by metal-to-metal or metal-to-nonmetal contact and is usually driven by the gradient of oxygen concentration between the gap and the bulk solution [48]. Crevice-induced corrosion or crevice-enhanced corrosion could occur due to corrosion products closing the crevice and establishing a new environment different from the bulk. The morphology of immersed high purity magnesium inside a crevice showed deep holes with rough river-like patterns, so one could argue that this is pitting corrosion induced by crevices [49].

Pitting and crevice corrosion occurs due to the fast corrosion of small-localised areas and is linked to the failure of a passive film. Pitted surfaces are often small at the surface and hidden by deposits from the process stream or corrosion products. The deposits form a barrier between the pit and the bulk solution, creating a local environment. They also make the pits difficult to see. The pits are often small but highly corrosive and they propagate downwards, perforating the matrix, though pits might also be shallow, elliptical, subsurface, undercutting or horizontal [50]. The environment in pits contains chlorides from body fluids, making the breakdown of the passive film more probable. With the reduction of protective film thickness, more magnesium is corroded and the pH increases as a result (see reaction equation 1.6). The local environment becomes more aggressive, and accelerates the corrosion process. Pitting can be detrimental to load-bearing magnesium implants as it can induce the formation of stress corrosion cracking and metal fatigue cracks, which can lead to failure of the implant [51]. Pitting is known to occur in magnesium and excessive pitting corrosion resulting from micropores could be detrimental.

Micropores can also be considered surface roughness. Large surface roughness has been shown to increase corrosion rates due to the instability of the protective layer over a large area [52]. An in-stable protective layer, in addition to increased localised degradation in magnesium alloys, reduces corrosion resistance significantly [53]. Alvarez *et al.* [54] have shown that higher surface roughness reduces general corrosion; they found that polished surfaces showed more pitting in the early stages of corrosion and higher pitting volumes than semi-polished samples. The semi-polished sample showed bigger radii of pits, but overall corroded less quickly compared to the polished sample. Surfaces with high roughness have more peaks and valleys. Those valleys are more susceptible to local pH change as hydroxide ions are formed and can be trapped in the valleys. The surface roughness makes local pH change more violent and passive layer breakdown is more probable. In the 24-hour immersion test, it was shown that rough surfaces

show more pitting corrosion, however when the alloy was held at anodic current, pitting occurred irrespective of the surface roughness [55]. Magnesium and its alloys are susceptible to pitting corrosion. Pores and rough surfaces may increase the chance of pitting corrosion but can reduce the general corrosion.

1.4 Objective

The addition of zinc has been shown to increase the corrosion resistance of extrusion-based 3D printed magnesium scaffolds. Zinc precipitates as secondary phases in a magnesium-based matrix. Micro-galvanic coupling occurs between the matrix and the secondary phases and promotes corrosion when the particles are not fine and homogeneously distributed. However, it has been shown that the corrosion resistance of extrusion-based 3D printed magnesium scaffolds benefits from the addition of zinc. The question that arises is, why the corrosion resistance of Mg-4Zn is higher than that of pure magnesium.

This thesis aims to provide new insight into the effect of the microstructure of Mg-4Zn scaffolds fabricated by material extrusion-based 3D printing. For this purpose, localised corrosion and electrochemistry techniques; scanning Kelvin probe force microscopy (SKPFM) and scanning electrochemical microscopy (SECM) will be used which are relatively new in this field. These techniques will be used to determine the influence of the microstructural features: secondary phase particles and micropores, which are the result of the manufacturing.

A brief description of the aforementioned techniques, sample preparation and the experimental conditions will be discussed in chapter 2: Materials and Methods. Chapter 3: Results and Discussion will explain the results obtained from the local electrochemical experiments and will link the influence of microstructural features to the corrosion behaviour. Future research suggestions will be given based on the results of this thesis in chapter 4: Research recommendations. And in the end, a summary of the obtained results and findings are given in chapter 5: Conclusion.

Chapter 2

Materials and Methods

This chapter aims to explain the experimental methods for the determination of the effect of microstructure on the corrosion of Mg-4Zn. In this thesis, several analytical techniques will be used. The basics of each technique; scanning electron microscopy (SEM), scanning Kelvin probe force microscopy (SKPFM) and scanning electrochemical microscopy (SECM), will briefly be discussed. To obtain more knowledge on the techniques, the reader is recommended to take a look at the references. In the experimental conditions section, the used materials for extrusion-based 3D printing will be described. In addition, the procedure for the determination of microstructure will be discussed. The scanning procedure for SKPFM and SECM will be explained, together with the treatment of raw data. Lastly, the preparation of r-SBF as an immersion solution for SECM measurements will be described.

2.1 Determination of the microstructure

Optical microscopy is a simple yet very convenient technique that uses visible light to obtain magnified images. There are only a few constrictions for samples to be viewed under the optical microscope. However, when interesting structural features are small, such as secondary phase particles, the magnification of optical light microscopes is a limitation. They are limited by low resolution ($\approx$ 200nm [56]) due to the large wavelength of visible light, electron microscopes were developed to gain higher resolution [57]. Therefore, scanning electron microscopy (SEM) will be used alongside optical microscopy.

Electron microscopy includes various types of microscopy, but all share the usage of an electron beam as a source. Electrons can interact with the sample in various ways, and create different signals as can be seen in figure 2.1. The most widely used signal after the interaction of the incident electron beam with the specimen is the secondary electron emission signal. The incident electron beam hits the surface of the specimen, causing it to ionise by the emission of loosely bound electrons. These are the secondary electrons and they possess low energy; 3-5 eV [58]. The electrons are detected by the secondary electron detector (SED) and give topographic information as they escape only from a few nanometers from the surface.

Another type of signal produced by irradiating a specimen with an incident electron beam is the characteristic X-rays. An incident electron can eject an electron out of its shell, the inner shell electron is then replaced by a higher energy outer shell electron. The difference in energy between the inner and outer shell electrons is released in the form of X-ray emission. Emitted X-rays pro-

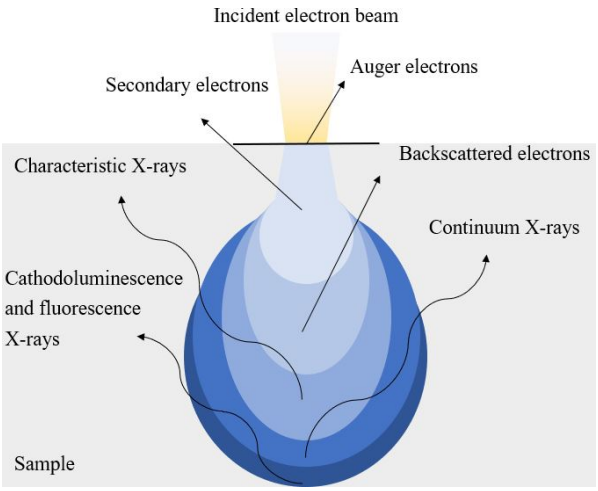

Figure 2.1: Electron interaction with matter and generation depth indication of the different types of signals generated.

vide elemental information used for elemental composition characterisation in energy-dispersive X-ray spectroscopy (EDS). Characteristic X-rays are emitted from deeper under the surface than secondary electrons for electron low electron energies. Therefore elemental composition does not directly correspond to surface features. SEM and EDS will be used for quick surface morphology and composition analysis of corrosion products.

The penetration depth of the electrons can be determined by models such as the Kanaya-Okayama model [59]. The maximum penetration depth of electrons R_{K-O} (nm) is defined as

$$R_{K-O} = \frac{27.6A}{\rho Z^{0.89}} E_0^{1.67} \tag{2.1}$$

where A is the atomic weight (g/mol), ρ is the material density (g/cm^3) Z is the atomic number, and E_0 is the initial electron energy (keV). The penetration depth is calculated for magnesium, zinc, oxygen, phosphor and calcium, shown in Table 2.1. Although the Kanaya-Okayama model is in agreement with experiments in the energy range of 10-1000 keV, it is used here to give an indication of penetration depth at 2 to 20 keV for the choice of electron energy. A high resolution is desired, which is obtained using high electron energies, but the electron energies should not penetrate the surface extensively, since composition will then not be corresponding to surface features.

SEM is a non-destructive technique that provides useful topographical and elemental information, however the main limitation is the requirement of a conductive sample since the electron beam can damage or charge the sample. Non-conductive samples, such as Mg-Zn scaffolds require to be coated before they can be analysed in SEM. The sample is not required to be coated when analysed with EDS.

2.2 The influence of secondary phases on the surface potential

The analysis of corrosion properties by polarisation curves and electrical impedance spectroscopy experiments (EIS) have proven highly suitable for the characterisation of the corrosion resistance of magnesium alloys. However, these techniques define the general corrosion and do not reveal anodic or cathodic contributions from features on the surface [60]. For the analysis of the effect of secondary phases on the corrosion, a local technique will be used: scanning Kelvin probe force microscopy (SKPFM).

Table 2.1: Penetration depth (nm) of various initial electron energies (keV) in magnesium, zinc oxygen, phosphor and calcium.

Initial electron energy	**Mg**	**Zn**	**O**	**P**	**Ca**
2	130	40	120	130	160
3	260	80	230	260	310
5	620	180	540	620	730
10	1980	570	1700	1970	2320
20	6290	1820	5430	6270	7380

SKPFM is a powerful technique to assist in understanding the possible corrosion processes associated with local features on surfaces when exposed to aggressive solutions. The SKPFM is a modified technique that combines atomic force microscopy (AFM) and associated techniques with scanning probe microscopy (SPM) with the scanning Kelvin probe (SKP). The topography is measured using the tapping mode of AFM. In the tapping mode, a cantilever with a sharp tip oscillates. As the probe approaches the surface, it is influenced by interaction forces between the surface and the probe. The interactions include Van der Waals- and electrostatic forces, in addition to dipole-dipole interactions. These forces cause the probe to reduce its vibration amplitude and is used to map surface morphology. The topography is measured in the forward pass of the probe, on the backwards pass the lift mode is used. In the lift mode, the tip is lifted to a certain distance above the surface, usually 100 nm, and the Volta-potential difference is measured. Therefore, the topography and contact potential distribution of a surface with inhomogeneities can be simultaneously mapped with high sensitivity.

The Volta- or contact potential difference is measured between two metals or alloys. The Volta-potential is the difference in electrostatic potential between two metals in contact and which are in thermodynamic equilibrium. It is defined as the electric potential difference between a point in the vacuum close to the surface of a metal and another point in the vacuum close to the surface of another metal [61]. When two dissimilar metals are brought into contact, electrons drift from the metal with the higher Fermi level to the metal with a lower Fermi level. The Fermi levels are equilibrated, leading to a measurable work function and the Volta-potential difference. The work function is defined as the energy needed to bring an electron from the Fermi level to the vacuum level. The work function (Φ) and the Volta-potential (Ψ) are linearly related:

$$\Phi = \overline{\mu} - zF\Psi \tag{2.2}$$

where ($\overline{\mu}$) is the electrochemical potential z is the valence, and F is the Faraday's constant.

When a material is in contact with the probe, electrons will flow from the material with a higher Fermi level to the material with a lower Fermi level, until an equilibrium is established, this can be seen in Figures 2.2a and b. A charge is applied to counter the flow of electrons to the material with a lower Fermi level (Figure 2.2c). The difference in contact potential to the probe can then be mapped over a whole surface. Metals with high work functions and Volta-potentials demonstrate high electrochemical nobility. Low work functions and Volta-potentials represent an increased tendency for electron transfer, indicating high electrochemical activity and thus these measured potentials can be used to reflect the corrosion properties. Therefore, the Volta-potential is used to indicate regions with varying nobility within a specimen, which reflects the behaviour of the specimen in fluids or ambient conditions. The corrosion potential does not always correlate with Volta-potential as the corrosion potential of a metal in an electrolyte reflects the true electrochemical nobility. The Volta-potential shows the strength of electrostatic fields generated between two metals and indicates only the tendency of a metal to undergo an electrochemical reaction.

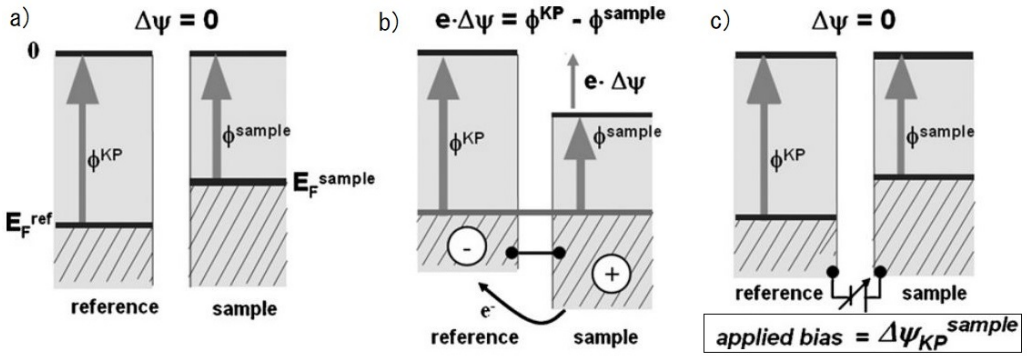

Figure 2.2: The Kelvin probe KP and sample are brought into contact. This results in a Volta-potential difference due to charge transfer by the equilibration of Fermi levels (b). An external bias is applied between the Kelvin probe and the to compensate the Volta potential difference, which leaves both surfaces uncharged (c) [62].

SKPFM provides thus an indication of the nobility of secondary phases relative to the matrix, which is important in determining the role in galvanic interactions. The ability for SKPFM to map corrosion tendency is used to locate preferential corrosion regions in a material [63]. It enables the identification of micro-galvanic interactions between the matrix and small secondary phase particles to be studied. The Volta-potential is highly sensitive to the environment and the surface condition of the tested materials and is not a constant parameter. The measured potential will differ depending on the relative humidity, temperature, sample preparation and scanning parameters [62]. SKPFM is a useful technique in determining only the relative properties of local cathodic or anodic sites [64]. The Volta-potential difference is a useful quantity for assessing the relative nobility of local microstructural features and is used to improve the understanding of localised corrosion at the micrometre scale. And recently, resolution at the nanometre scale has been achieved [65].

2.3 The influence of micropores of porous scaffolds

The effect of pores on the corrosion can be evaluated using scanning electrochemical microscopy (SECM). SECM is used to measure, characterise and evaluate localised corrosion processes and electrochemical activity distributions in surfaces with high spatial resolution [66]. SECM is a near-field scanning technique using an ultramicroelectrode (UME) to detect electrochemical activity in heterogeneous systems, such as porous surfaces.

SECM combines the high spatial resolution of scanning microscope techniques with electrochemical selectivity provided by the use of an electrode as the probe. This allows for *in situ* surface characterisation with a resolution in the micrometre range. The components of the SECM are the UME as the working electrode, a reference electrode and a counter electrode to complete the electrochemical cell. The substrate (sample to be studied) can also act as a secondary working electrode. A bipotentiostat is connected to the cell control the experimental conditions. The UME consists of an inert electrode material such as carbon fibres or metal wires, surrounded by an insulating shield of glass. By applying a potential in the UME, a redox process can take place at the tip of the UME resulting in a measurable current. The current can be related to the concentration of the redox species involved in the reaction at the tip, with the use of the following equation:

$$i_{T,\infty} = 4nFDca \tag{2.3}$$

where $i_{T,\infty}$ is the steady-state current (A), n is the number of electrons transferred at the UME

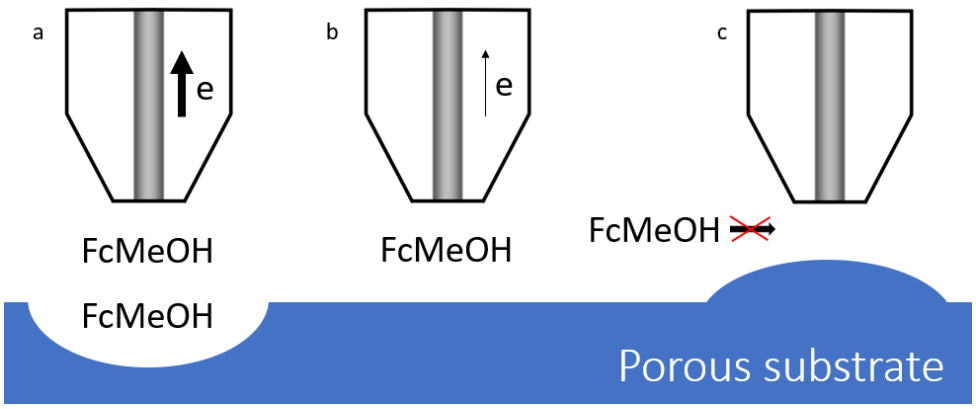

Figure 2.3: Schematic diagram of the UME with ferrocenemethanol (FcMeOH) as the redox mediator in the constant height mode. When the tip is far from the surface, due to a local valley a high current can be measured (a). When the tip is close to the surface, some ferrocenemethanol diffusion is blocked and a current smaller than the steady-state limiting current is measured (b). When the tip encounters a local increase in surface, the diffusion of ferrocenemethanol is blocked and no current is measured (c).

tip, F is the Faraday constant (96485 C mol^{-1}), a is the microelectrode radius (m), D is the diffusion coefficient of the reducible species (m^2 s^{-1}), and c is its concentration (mol). Therefore, the current can be used for the quantification of the redox species.

The sample generation/ tip collection (SG/TC) mode can be combined with the feedback mode to correlate localised corrosion with surface morphology. The feedback mode requires the addition of a redox mediator, which generally involves a one-electron heterogeneous reaction [66]. A frequently chosen mediator is ferrocenemethanol ($C_{11}H_{12}FeO$ or FcMeOH) for its reversible oxidation, according to:

$$\mathrm{FcMeOH} \longleftrightarrow \mathrm{FcMeOH^+} + \mathrm{e^-} \tag{2.4}$$

The redox potential of the oxidation occurs at +0.5 V vs. Ag/AgCl, KCl (saturated) to the open circuit potential. The reaction is controlled by the diffusion of the oxidising species from the bulk through the solution to the surface, which can be seen in Figure 2.3a on the left side. When the tip of the UME moves close to the surface, the steady-state current is smaller than the limiting current, resulting from a blockage of diffusion of the ferrocenemethanol to the surface on an insulating surface, such as seen in Figure 2.3b. The current decreases as the tip approaches the surface and will go to zero when the distance between the tip and surface approaches zero, which can be seen in Figure 2.3c. The negative feedback mode can thus be used to measure local changes of the surface topography.

Not only ferrocenemethanol but also hydrogen can be mapped which is the SG/TC mode. Hydrogen originates from the corrosion of magnesium and it can be oxidised back at the tip as follows:

$$\mathrm{H_2} \longrightarrow 2\,\mathrm{H^+} + 2\,\mathrm{e^-} \tag{2.5}$$

With the combination of measuring hydrogen evolution and morphology, a correlation can be made between surface heterogeneities and electrochemical activity. For the Mg-4Zn scaffolds, the heterogeneity comprises of different surface heights due to the microporous surface adn the formation of a corrosion layer. The SECM is used for *in vitro* and *in vivo* testing. For *in vitro* testing, a fluid should be chosen close to its final application; the human body.

Solution for *in vitro* immersion

To mimic the environment in the body, simulated body fluid (SBF) can be used. Several kinds of SBFs are used in *in vitro* studies, such as conventional or Kokubo (c-SBF), revised (r-SBF), ionised (i-SBF) and modernised (m-SBF). Furthermore, Hanks' balanced salt solution (HBSS) is also frequently used. Several types of body fluids are thus probable to serve the purpose of recreating an environment close to human blood. R-SBF will be used as the solution since the nominal ion concentrations are closest to those of blood plasma as shown in Table 2.2.

The ions in SBF can react and form various reaction products. These reactants can also react with the magnesium and zinc substrate and form other corrosion products next to the magnesium hydroxide. The possible formation of hydroxyapatite is the main reason SBF is used. Hydroxyapatite is considered the most thermodynamically stable in a physiological environment. However, other calcium-phosphorous compounds have been regarded as precursors of hydroxyapatite or the metastable phases. These compounds include dicalcium phosphate ($CaHPO_4$, DCPD), tricalcium phosphate ($Ca_3(PO_4)_2$, TCP) and octacalcium phosphate ($Ca_8(HPO_4)_2(PO_4)_4$, OCP), formed according to the following reactions [67, 68]:

$$Ca^{2+} + HPO_4{}^{-} \longrightarrow Ca_5(PO_4) \tag{2.6}$$

$$3\,Ca^{2+} + 2\,PO_4{}^{3-} + \longrightarrow Ca_3(PO_4)_2 \tag{2.7}$$

$$7\,Ca^{2+} + 4\,PO_4{}^{3-} + HPO_4{}^{-} + 5\,H_2 \longrightarrow Ca_7H_2(PO_4)_6 \cdot 5\,H_2O \tag{2.8}$$

The corrosion products are important as they influence the stability of the passive layer. A passive layer of only magnesium hydroxide is presumed to break down. The addition of stable corrosion products can therefore stabilise the corrosion layer and diminish the breakdown.

Table 2.2: Nominal ion concentrations (mM) of the c-, r-, i and m-SBF compared human blood plasma in total and dissociated mounts [69].

Ion	**Blood plasma Total**	**Blood plasma Dissociated**	**c-SBF**	**r-SBF**	**i-SBF**	**m-SBF**
Na^+	142	142	142	142	142	142
K^+	5	5	5	5	5	5
Mg^{2+}	1.5	1	1.5	1.5	1	1.5
Ca^{2+}	2.5	1.3	2.5	2.5	1.6	2.5
Cl^-	103	103	147.8	103	103	103
$HCO_3{}^-$	27	27	4.2	27	27	10
$HPO_4{}^{2-}$	1	1	1	1	1	1
$SO_4{}^{2-}$	0.5	0.5	0.5	0.5	0.5	0.5

2.4 Experimental conditions

Porous scaffolds production using material extrusion-based 3D printing

Magnesium porous scaffolds were 3D printed according to [70] by J. Dong. Pure Mg powder (impurity <0.01 wt%) and Mg-Zn powder (95.6 wt% Mg, 4.1 % Zn and 0.3 wt% impurities) with a spherical particle shape and median particle sizes of 44.96 µm and 37.7 µm, respectively, were used as the starting materials (Tangshan Weihao Magnesium Powder Co., China). The powder particles were mixed with a binder system of hexane and polyisobutylene polymer (molecular weight ≈ 500000, Sigma Aldrich, Germany) to form the ink. The ink consisted of 50 vol.% powder particles and was then loaded on a 3D Bioscaffolder printer in a syringe. The ink was printed with a lay-down pattern of 0°/90°/0° in a cylindrical porous architecture by extrusion of the ink under high pressure (140-160 kPa). The printed scaffolds were then exposed to high temperatures for the de-binding of the metal particles from the binder system and to sinter the loose metal particles.

Microstructure determination

The scaffolds were embedded in resin using a mould of 3 cm in diameter. The embedded scaffolds were sanded using P2000 grit (Struers SiC Foil, Grit 2000 (US #1000) 200 mm) sandpaper followed by P4000 grit sandpaper (Struers SIC Foil, Grit 4000 (US #1200) 200 mm). Care was taken to avoid using water and isopropanol was used as a lubricant during sanding instead. After sanding, the samples were cleaned with isopropanol in an ultrasonic bath for 10 minutes. The samples were polished using 1 µm polishing liquid (Struers DP-Paste P, 1 µm) on a porous neoprene polishing cloth (Struers MD-Chem). The polishing liquid was removed with water, then immediately rinsed with isopropanol and ultrasonically cleaned again. The polished surfaces were etched with a mixture of nitric acid (HNO_3, Sigma-Aldrich), acetic acid (CH_3CO_2H, Sigma-Aldrich), water (Mili-Q ultra-pure water), and ethanol (C_2H_5OH, Sigma-Aldrich) at the volume ratio of 1:3:4:12.

The average grain size was determined using the line intercept method as described in ASTM E112-13 'Standard test methods for determining average grain size' [71]. Since the line intercept method is not adequate with porous materials an adjustment was made with the measurement of a line; the pores intercepting the line were measured and subtracted from the width of the line, and the line intercept method was continued. The average strut and pore widths were measured using ImageJ on optical microscopy images taken with the Keyence VHX 6000 Digital Microscope. The average secondary phase size was measured using ImageJ on SEM images, which were taken with the Jeol JSM-IT100 InTouchScope^{TM} Scanning Electron Microscope. For SEM measurements, the initial electron energy of 20 keV electron was used when the surface was gold-sputtered.

Preparations for SKPFM measurements

The scaffolds were sanded and polished as described in the previous section. The polished scaffolds were etched to reveal the secondary phase particles, but etching was later dismissed as it was not necessary and it could change the surface potential. Volta-potential maps were obtained on the same day as the sample preparation using a Bruker Dimension Edge^{TM} AFM with PtIr (Bruker, SCM-PIT-V2) tips on surface potential mode. The measurements were performed at the height of 100 nm under a bias potential of 6V. For all the scanning parameters, see table A.2 in Appendix A.

The Volta-potentials were measured on Mg-4Zn scaffolds, a pure magnesium scaffold and an immersed Mg-4Zn scaffold by 4.75 hours of immersion in water. Copper tape was applied at

Table 2.3: Reagents for the preparations of r-SBF.

Reagents	**Chemical formula reagents**	**Concentration (mg/L)**
Sodium chloride	NaCl	5403
Sodium bicarbonate	$NaHCO_3$	740
Sodium carbonate	Na_2CO_3	2046
Potassium chloride	KCl	225
Potassium phosphate dibasic trihydrate	$K_2HPO_4 \cdot 3\,H_2O$	230
Magnesium chloride hexahydrate	$MgCl_2 \cdot 6\,H_2O$	311
HEPES (2-[4-(2-hydroxyethyl)-1-piperazinyl]ethanesulfonic acid)	$C_8H_{18}N_2O_4S$	11928
Calcium chloride	CaCl2	293
	$CaCl_2 \cdot 2\,H_2O$ (If no $CaCl_2$ available)	388
Sodium sulfate	Na_2SO_4	72
Sodium hydroxide	1.0 M NaOH	800

the edges of the scaffolds to make contact with the stage. The immersed scaffold was dried with compressed air before being scanned. To compare nobility, an n-doped silicon substrate with patterned islands of aluminium surrounded by a gold interconnects (PFKPFM-SMPL by Bruker) was measured additionally. The obtained maps were read and processed using the Gwyddion software (Czech Metrology Institute, version 2.58). Gwyddion was used to remove horizontal scars, noise and the extreme positive and negative values from the scale to highlight the difference in surface potential of microstructural features. Further analysis was done on raw maps to show potential profiles of microstructural features.

Preparations for SECM measurements

For the immersion of the scaffolds, r-SBF was used with the addition of 0.5 mM ferrocenemethanol as a redox mediator. The r-SBF was prepared as described by Oyane *et al.* [69], with the difference of using $CaCl_2 \cdot 2\,H_2O$ instead of $CaCl_2$. The quantity was adjusted accordingly in order to not change the salt contents. All salts were sequentially added after the previously added salt was dissolved, in the sequence of Table 2.3 which also shows the concentration of species in r-SBF. All chemicals were purchased from Sigma-Aldrich or J.T.Baker and were used as received. The beaker was heated in a water bath as shown in Figure 2.4 and kept at a constant temperature of 37°C using a thermometer connected to the heating plate. After preparation, it was stored in a cooled atmosphere and used within a month of preparation.

Using an analytical balance, 21.6 mg ferrocenemethanol was measured, added to 40 mL of r-SBF and sonicated for half an hour to dissolve it. The solution was transferred to a 50 mL volumetric glass flask and filled to 50 mL with r-SBF. Samples were sanded and polished as described before. Translucent tape was placed around the embedded sample to form the container for the r-SBF. In the created cell, 5 mL of the 0.5 mM ferrocenemethanol in r-SBF solution was added. The whole polished surface would be exposed to the solution, which is approximately 1 cm^2 with alternating areas of strut and epoxy resin. The sample was fixed to the stage with double-sided tape and a bubble level was used to level the sample followed by three-point levelling, which was later replaced by levelling using a bubble level only. The UME had an inner platinum wire with a 10 µm diameter surrounded by glass with a diameter of 100 µm and

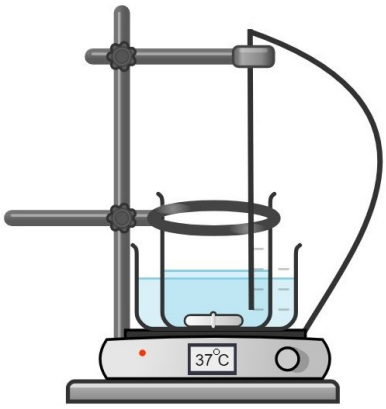

Figure 2.4: The set-up used for the preparation of r-SBF, where the heating plate with an attached thermometer was used for the constant temperature of 37°C.

RG(=r/D)=10. A platinum sheet of approximately 5 by 10 mm and an Ag/AgCl,(3 M) KCl were used as the counter and reference electrodes respectively. Electrodes were cleaned before being fixed in the Scanning Electrochemical workstation (Uniscan Model 370) with a Uniscan PG580R Potentiostat-galvanostat inside a Faraday cage and controlled using the M370 program. The UME was cleaned by performing ten cycles of cyclic voltammetry in 0.5 M sulfuric acid between -1 to 1 V.

Cyclic voltammograms were taken in the ferrocenomethanol/r-SBF solution far above the surface, so it was not influenced by the substrate. Cyclic voltammograms were taken to determine the limiting current and to examine whether the tip was contaminated. The UME was placed above the sample and lowered to approximately 1-3 mm. SECM approach curves were made on tape that covered the surface, directly on the strut or on the resin by lowering it until the current decreased to 88%, which corresponded to an approximate distance of 20 µm above the surface. Line scans were made with a step size of either 2.5, 5 or 10 µm over a distance of 600 to 2500 µm. The tip scanned the surface in a horizontal direction, while the samples were set with the struts in the vertical direction. This orientation ensured that both resin and struts were scanned. For all the scanning parameters, see table A.1 in Appendix A.

Line scans were taken at 0.5 V for the detection of ferrocenemethanol and -0.1 V for the detection of hydrogen. The measured current when detecting ferrocenemethanol was normalised by dividing the measured current by the steady-state diffusion-controlled limiting current. Normalised currents above 1 are obtained when the surface is active and/or conductive, while currents below 1 are obtained when the surface is inactive and or non-conductive. In this way, current variations can be attributed to variations in topography. Ferrocenemethanol is detected by the diffusion of the bulk electrolyte to the tip. A large amount of ferrocenemethanol then indicates a larger distance between the tip and sample and a small amount of ferrocenemethanol indicates a small distance. In this way, the evolution in topography was visualised. The amount of detected hydrogen was calculated using a=5E-6 m, D=4.25E-9 m^2s^{-1} [72], n=2 and Equation 2.3.

To determine the influence of the passive layer on the corrosion, the corrosion products were characterised by EDS, X-ray diffraction (XRD) and Fourier-transform infrared spectroscopy (FTIR). EDS is used for the composition, FTIR is used for the analysis of bonds and XRD is used for the structure of the corrosion products. For EDS measurements, the initial electron energy of 5 keV electron was used, since 20 keV would penetrate the surface extensively and energies lower than 5 keV would reduce the resolution drastically.

Chapter 3

Results and Discussion

This section shows the results of the influence of microstructure on the corrosion of 3D printed Mg-4Zn porous scaffolds. First, the structure (strut and macropore size) of the 3D printed scaffolds will be discussed. The microstructure will be characterised, which includes grain size, micropore size and secondary phase particle size and its composition. The influence of the secondary phase particles will be analysed using the surface potential maps made using SKPFM on pure magnesium and Mg-4Zn scaffolds. The influence of micropores will be evaluated using line scans made using SECM. Lastly, the composition of the corrosion products will be discussed.

3.1 Structure of 3D printed Mg-4Zn porous scaffolds

Figure 3.1 shows the structure of a 0°/90°/0° 3D printed magnesium scaffold. Macropores are found between the struts, as indicated in 3.1a while micropores are found within a strut as the result of de-binding of the polyisobutylene polymer. Figure 3.1b shows the surface of the scaffold where separate metal powder particles can be distinguished and micropores can be seen between them. The porosity of the scaffolds were 50.3 ± 3.4%, measured by J.Dong.

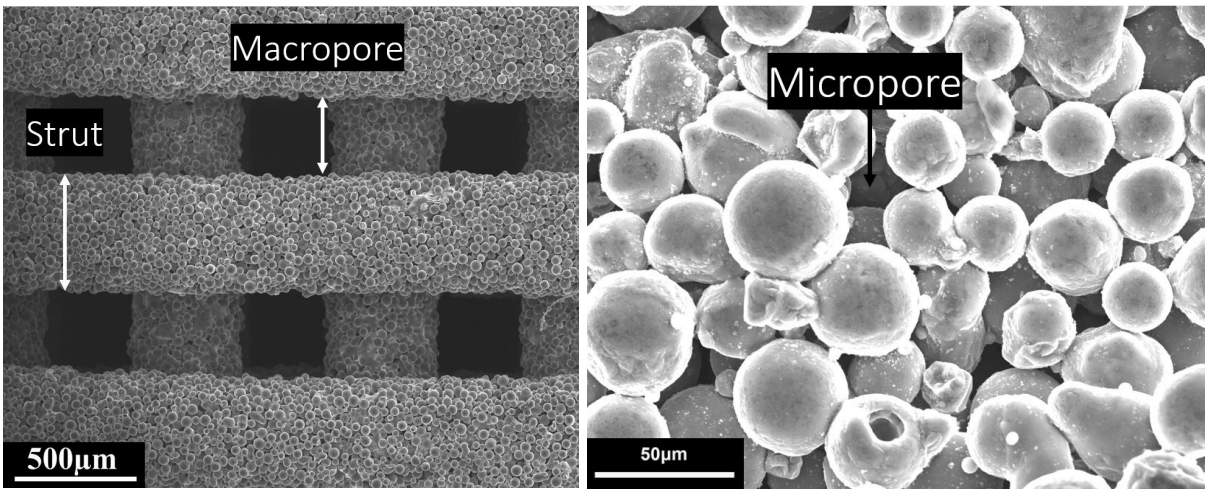

(a) (b)

Figure 3.1: SEM images of an as sintered structure of an extrusion-based 3D printed Mg-Zn scaffold at (a) 30x and (b) 500x magnification.

Table 3.1: Average of strut and macropore size, standard deviation and the respective number of species.

	Mean (µm)	**Standard deviation (µm)**	**Number of measurements**
Strut size MgZn-1	420	90	50
Strut size MgZn-2	490	60	50
Strut size MgZn-3	440	40	65
Strut size Pure magnesium	450	30	50
Macropore size MgZn-1	330	40	50
Macropore size MgZn-2	190	50	50
Macropore size MgZn-3	380	50	62
Macropore size pure magnesium	420	40	50

Three Mg-4Zn scaffolds (numbered 1-3) and a pure magnesium were printed on different moments, causing them to be printed with different nozzle diameters. The strut width and macropore widths were measured with ImageJ on optical microscopy images, which can be found in Table 3.1. Differences in macropore and strut dimensions are not features caused by the manufacturing type, but rather as the consequences of printing parameters, which did not affect the microstructure.

3.2 Microstructure of 3D printed porous Mg-4Zn scaffolds

Microstructural features considered to influence the corrosion properties of 3D printed Mg-4Zn were the sizes of grains, secondary phases and micropores present. The average grain size was determined using the line intercept with adjustments; the pores intercepting the line were measured and subtracted from the width of the line, and the line intercept method was continued. The resulting grain size was determined to be 25 ± 5 µm (*n=251*).

Secondary phase particles precipitated mostly on the grain boundaries, but some were present on the interior of grains. The secondary phase particles could be seen on etched samples after gold sputtering in SEM, see Figure 3.2. On optical microscopy images, they are less pronounced but could still be seen. The diameter of secondary phase particles was determined using ImageJ on SEM images to be 0.6 ± 0.3 µm (*n=50*).

Scaffolds were set in clear epoxy resin to prevent moisture and polishing liquid from getting trapped in micropores. All samples were set in epoxy resin using a mould size of 3 cm in diameter. The macro- and micropores were filled under the pressure of 2 bars whilst the epoxy resin cured. As the epoxy resin cured, it caused volumetric contraction of the resin. This contraction can be seen in Figure 3.2 in the micropores as the resin does not fill the whole pore.

The total composition of the scaffolds is Mg-4Zn (weight percent). The composition of secondary phase did not become apparent from EDS analysis, as the penetration depth exceeded the diameter of most secondary phase particles, even at 5 kV. Using electron energies less than 5 kV resulted in low resolution. The composition of secondary phase particles was determined to be $MgZn_2$ by Dong *et al.* [73] using XRD, see Figure B.1 in Appendix B for the diffractogram. Using 4 wt.% zinc (1.5 at.% zinc and 2.25 at.% $MgZn_2$), assuming spherical particles with a radius of 0.3 µm and the atomic radii of magnesium and zinc 160 and 133 pm respectively [74], the number density of secondary phase particles was calculated to be 7 secondary phase particles per 100 μm^2.

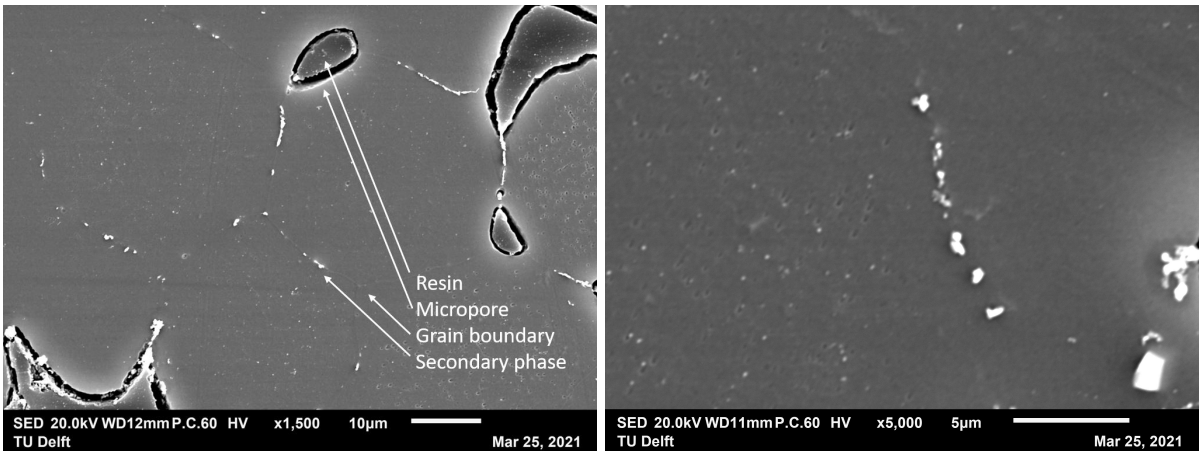

(a) (b)

Figure 3.2: SEM image of a cross-section of an etched Mg-4Zn scaffold showing micropores, grain boundaries and micropores at 1500x magnification (a) and 5000x magnification showing a row of secondary phase particles (b).

In the estimation of the number density of secondary phase particles, a circular shape was considered. The shape of the secondary phase particles are not perfectly spherical, as can be seen in Figure 3.2b, but a spherical shape defines the average shape sufficiently. It was assumed that zinc was only present in precipitated secondary phase particles, but not all zinc is precipitated as particles, some zinc is dissolved in the matrix, which estimates 7 secondary phase particles per 100 µm^2 too high.

The shape of the micropores on the cross-section of the scaffold was non-spherical. Only the largest horizontal widths of pores were measured as can be seen by the white bars in Figure 3.3 to ensure reproducibility. The micropore size was determined to be 14 ±11 µm (*n=100*), however care must be taken not to consider this a fixed number since micropore sizes ranged between 1 and 70 µm.

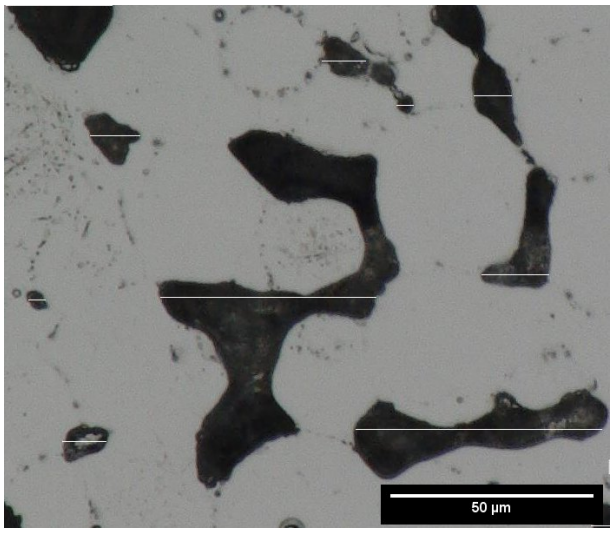

Figure 3.3: Optical microscopy image of a cross-section of a Mg-4Zn scaffold showing the size determination of micropores.

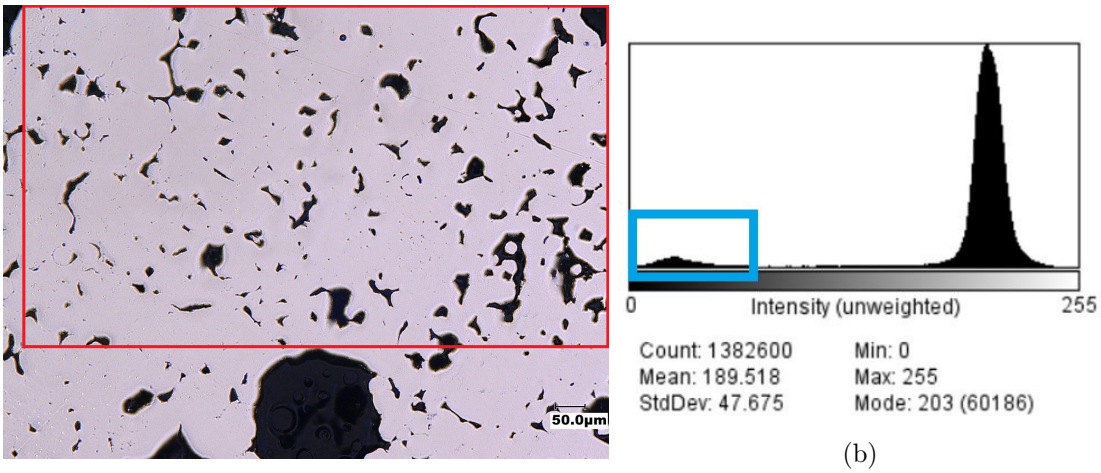

(a) (b)

Figure 3.4: (a) Optical microscopy image of the cross-section of a Mg-4Zn scaffold and (b) histogram of the red indicated square in (a). The blue square indicates the darker colour in the histogram used for the determination of micropore area, which is 7.4% for the area in the red square.

To estimate the number density of micropores, the area was measured using ImageJ. The dark colours indicate the micropore area in Figure 3.4a. The pixel count in the lower spectrum was divided by the total amount of pixels and this resulted in a percentage of the area corresponding to micropores, which was approximately 5%. Using the average micropore size, an estimation of the micropore number density can be made. The micropores were generated randomly during solvent de-binding, thus this percentage could deviate depending on its location. Using a micropore area percentage of 5%, the micropore diameter of 14 µm and a circular shape, the number density was estimated to be 325 micropores per mm^2.

Micropores form an interconnected network due to solvent extraction. Due to the interconnected network, the length can be greater than the dimensions of the scaffolds. Sanding and polishing scaffolds will lead to cross-sections where micropores are randomly cut through. The average of measured micropore dimension was based on those randomly cut through cross-sections. Micropore dimensions were measured as the longest horizontal distance within a pore. Thus, the measured micropore dimensions will not reflect their true size well. For the determination of micropore number density, a circular shape was assumed. A circular shape did not define the true shape. Nevertheless, the micropore size and number density measured on the cross-section are still convenient, since they were used in SECM where local valleys could be correlated to micropores.

3.3 The influence of secondary phases on the corrosion of Mg-4Zn

Surface potential differences were measured by SKPFM to correlate secondary phases with corrosion behaviour. The Volta-potential provides only an indication of the relative potential of secondary phase particles. There is no direct implication of whether a secondary phase particle with a positive Volta-potential acts as a local cathode for micro-galvanic corrosion. To solve this, the PFKPFM-SMPL from Bruker was scanned to correlate the signs of measured potential with anodic or cathodic behaviour. The topographical and the Volta-potential map can be found in Figure 3.5, where the aluminium island can be seen on the left and the gold on the right, separated by a valley of n-doped silicon. The valley is approximately 50 µm deep as can be seen in the mean profile graph in Figure 3.5c. The measured potential of the PFKPFM-SMPL is dependent on the scan height [75] and although gold is topographically higher, the two potentials can still be compared. Gold has its potential at the upper end of the scale, however, the potential of aluminium does not immediately become clear. The topographical map is taken at the forward passing of the cantilever over the surface i.e. left to right, while the Volta-potential map is taken at the backwards passing of the cantilever. This results in a shadow of the tip on the left side of topographical features. There is a shadow due to the steep decline in height which separates the aluminium from gold. The Volta-potential map of PFKPFM-SMPL is not as sharp as the

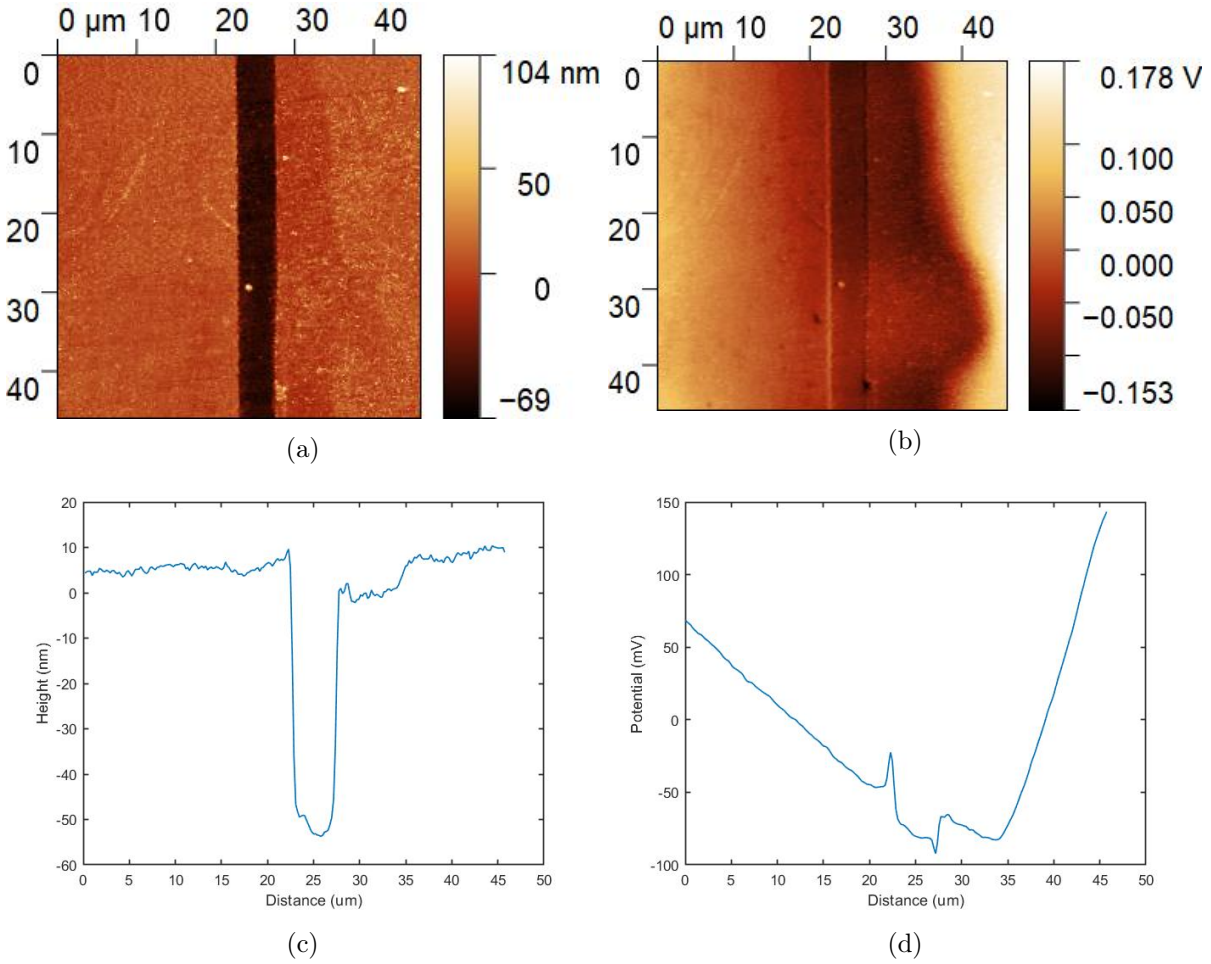

Figure 3.5: SKPFM result showing a topographical map (a) and a Volta-potential (b) map of the PFKPFM-SMPL with the mean profiles of topography (c) and Volta-potential (d). The aluminium island is seen on the left side with gold on the right, separated by a gap of n-doped silicon.

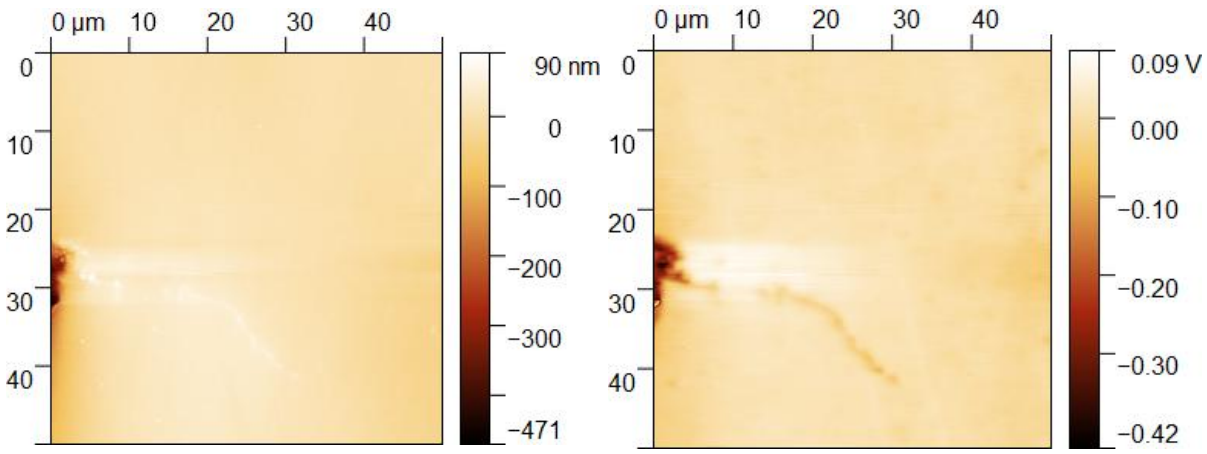

(a) (b)

Figure 3.6: SKPFM result showing a topographical map (a) and a Volta-potential (b) of a pure magnesium scaffold with a micropore on the left.

topographical map. When the scanning area is increased, the same gradient is seen. In the literature, however, the measured potentials on a 30 µm line are sharper and without gradient [75]. The gradient in potential might be due to contamination on the sample or due to a passive layer formed on aluminium since aluminium is, just like magnesium, very prone to corrosion. The formation of aluminium oxide (Al_2O_3) could shift the potential to higher values as it is more noble than aluminium. Gold is noble and shows high potential and thus it is confirmed that a high potential indicates high nobility.

3.3.1 The surface potential of Mg-4Zn compared to pure magnesium

A pure magnesium scaffold was scanned to compare with the Mg-4Zn scaffold since it does not have any precipitates of secondary phase particles. The pure magnesium scaffold was fabricated using the same technique and similar parameters to the alloy. The magnesium scaffolds were therefore expected to show similar micropore dimensions and grain sizes. Figure 3.6a shows the topography and Figure 3.6b shows the Volta-potential map of a polished magnesium scaffold. The artefact on the middle left is a micropore which was measured here to ensure some topographical differences, as such an artefact shows that the scan was completed successfully.

The scale shows a range of -420 mV to 90 mV with the micropore being the main cause of that range into the negative values. The micropore is filled with resin, though as presented from the SEM image from Figure 3.2, the edges of the pore are not filled, causing a local valley which displays as a low local potential. The average of the top 19.5 µm (100/256 pixels) was determined to be -0.5 ± 300 µV.

Figure 3.7 shows the topography and Volta-potential map of a Mg-4Zn scaffold. From the topographic map, it is possible to distinguish grain boundaries and precipitated secondary phases along the grain boundaries. The secondary phase particles appear at elevated height compared to the magnesium-based matrix due to the polishing and etching steps as a part of sample preparation, which attacks the softer magnesium-based matrix to a greater extent. From the Volta-potential map, an increase in potential corresponding to secondary phase particles can be seen. The Volta-potential map in Figure 3.7c is the same map without horizontal scars removed. The removal of noise does not affect the measured values, it was removed to emphasise the increased potential of the secondary phase particles in the Volta-potential map. The scale shows a range of -287mV to 614 mV in Figure 3.7c, which are the maximum and minimum measured

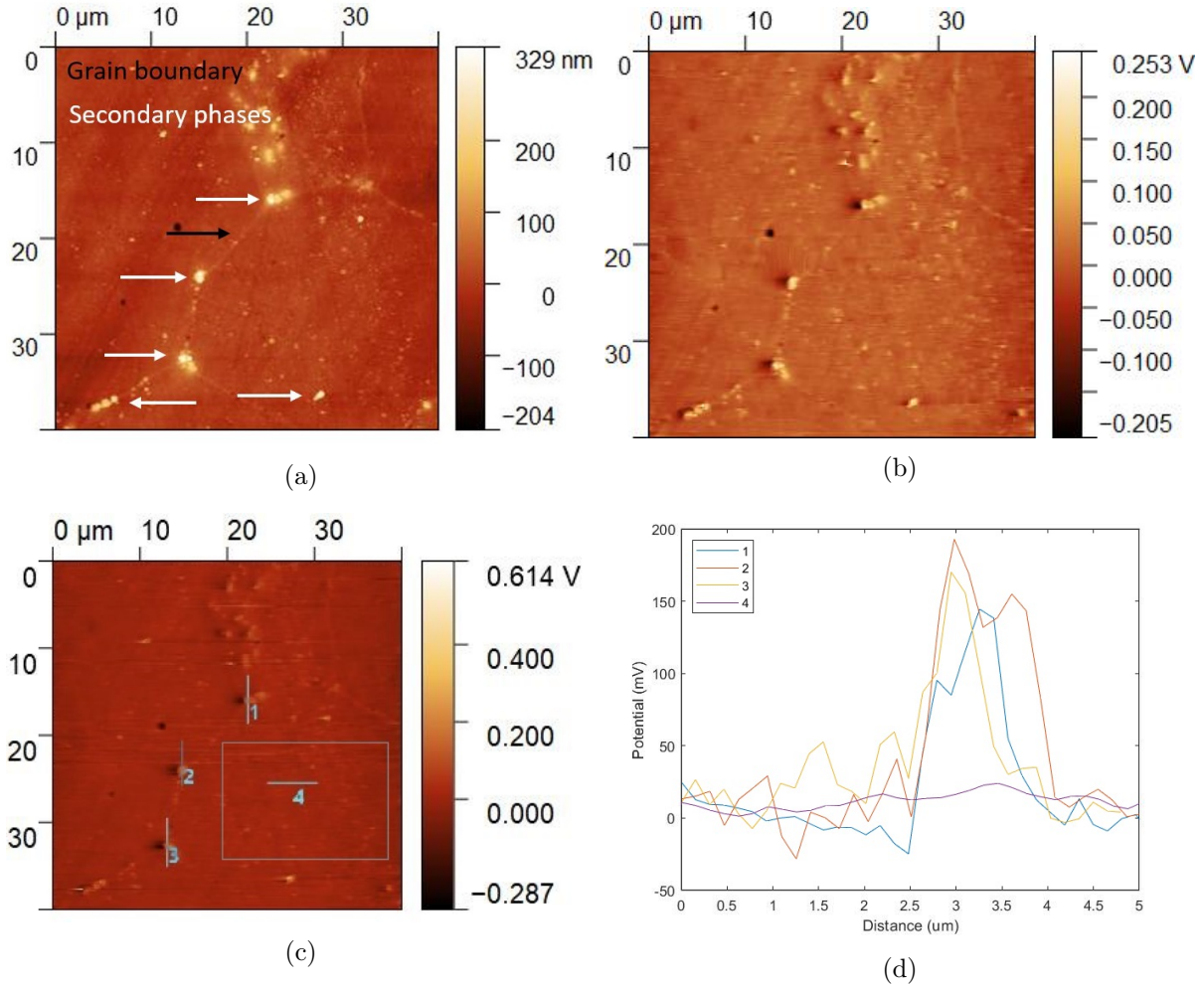

Figure 3.7: SKPFM result showing a topographical map (a), a Volta-potential (b), (c) Potential map of raw data with (d) voltage profiles through secondary phase particles at the grain boundary of an etched Mg-4Zn scaffold. The local maximum corresponds to the precipitate's potential. The rectangle indicates the area in the grain boundary where the mean value was determined to be 3 ± 10 mV.

values over the whole map. The magnesium matrix is relatively dark and the potential of the interior of the grain was measured to be 3 ± 10 mV.

The secondary phase particles and the grain boundaries show higher potential values, indicating a high nobility. Figure 3.7d shows Volta-potential line profiles of three $MgZn_2$ secondary phase particles (lines 1-3) and a line profile of the magnesium matrix in the middle of a grain (line 4). Line 4 shows a consistent potential at the interior of the grain. Lines 1 and 2 go through two secondary phase particles, giving rise to two local maxima. Line 3 intercepts one big secondary phase particle and a number of smaller ones. The grain boundary is also intercepted, therefore peaks in potential are seen before and after the secondary phase particles. Since the profiles are taken on raw data maps, horizontal scars were still present, resulting in noise in the line profiles that go through the matrix. The line profiles through secondary phase particles were taken vertically to reduce the shadow effect. Secondary phase particles showed an average increase of 140 ± 50 mV (*n=20*) compared to the matrix. Secondary phases show higher nobility than the matrix and will act cathodically. The magnesium-based matrix in Mg-4Zn showed higher potential than pure magnesium scaffolds (3 mV compared to -0.5 µV). This higher potential might be due to the presence of zinc in the matrix of Mg-4Zn or due to the presence of corrosion

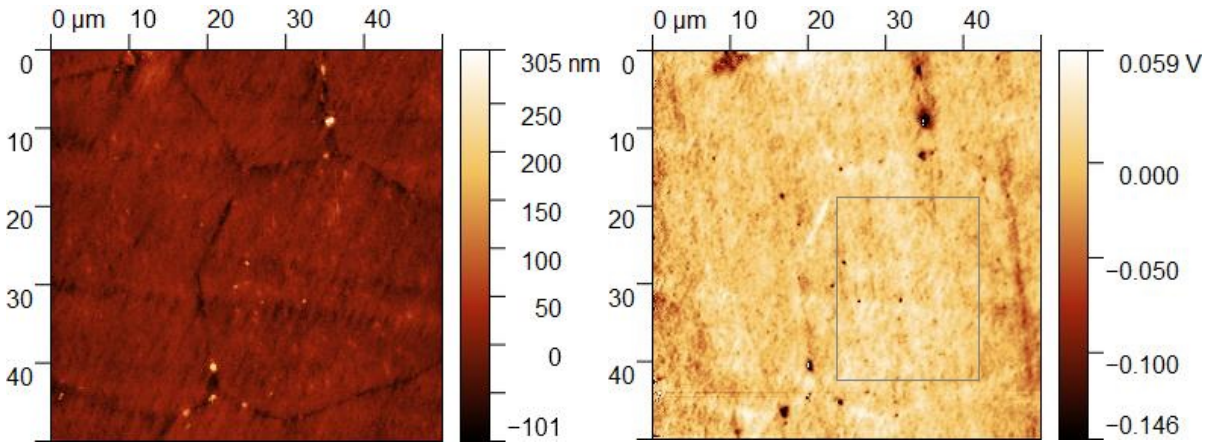

(a) (b)

Figure 3.8: SKPFM results showing a topographical map (a) a Volta-potential (b) of a lightly corroded scaffold. The square indicates the area in the grain boundary where the mean value was determined to be 7 ±7 mV.

products as a result of polishing or etching.

3.3.2 The surface potential of corroded Mg-4Zn

Secondary phase particles showed higher potential and are thus nobler than the matrix. However, the opposite was also measured where the secondary phase appears to show a lower potential than the matrix. This occurred when the samples were corroded. The samples were imperceptibly corroded due to the polishing liquid containing water and polishing for an extended amount of time. Volta-Potential maps showed evidence of corrosion nonetheless. The samples were also corroded due to immersion in water for 4.75 hours to compare the effect of corrosion products.

The topography map in Figure 3.8a shows a rougher surface than the previous topography maps due to polishing for an extended amount of time. The height of the secondary phase particles were 190 ± 50 nm (n=6), which is lower than 280 ± 50 nm (n=8) for the secondary phase particles in Figure 3.7a. This decrease of height might be due to the ethant's attack on the matrix in Figure 3.7a, the friction during polishing for an extended amount of time or the formation of magnesium oxide on the surface. In the Volta-potential map in Figure 3.8b, it is seen that the secondary phase particles show a much lower potential than the magnesium-based matrix. When taking a closer look, a peak in potential can be seen in the secondary phase particle at (35,9) and in (20,40) µm. The secondary phase particle at (35,9) µm consisted of two particles, which can be seen in the topographical maps.

The magnesium-based matrix in the grain has an average of 7 ± 7 mV which is higher than the not corroded sample in Figure 3.7, i.e. of 3 ± 10 mV. The elevation in the potential of the matrix indicates that a small layer of corrosion product has formed on the surface, which is nobler than the bare magnesium-based matrix. Although the two average potentials are in the same order of magnitude and taking the standard deviation into account, they do not differ much.

The secondary phase particle showed an area of decreased potential greater than the particle size. It is suspected that corrosion products had formed on and around the secondary phase particle. The corrosion products consist mainly of magnesium oxide, which is non-conductive. Therefore, the shift from high potential to lower potential of the secondary phase is due to the covering of the

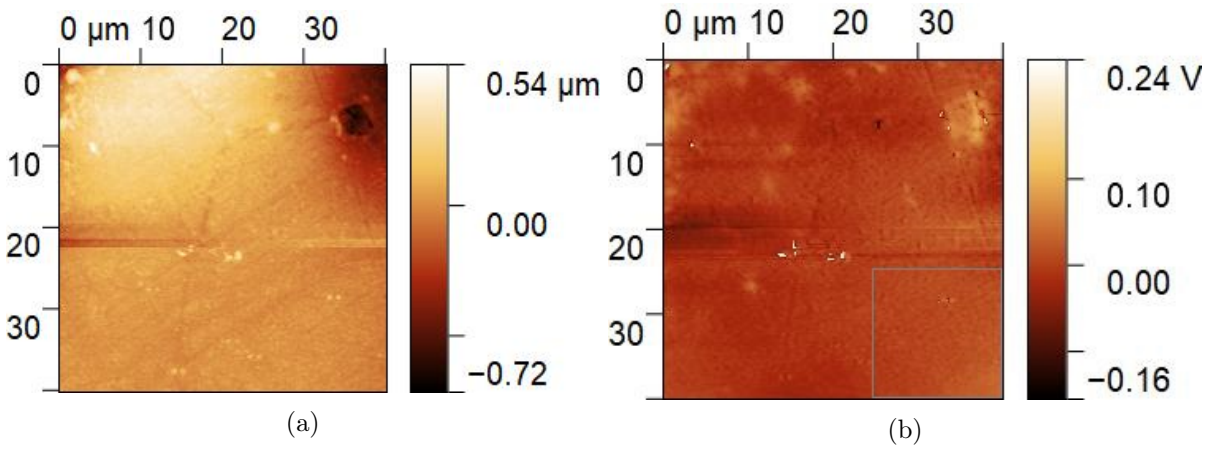

Figure 3.9: SKPFM result showing a topographical map (a) and a Volta-potential (b) of a corroded surface of a Mg-4Zn scaffold, after 4.75 hours of immersion in water.

secondary phase with a non-conductive oxide layer. The matrix showed an increased potential, yet the secondary phases show a decreased potential due to the corrosion of the surface. It is thought that the area surrounding the particle shows lower potential compared to the matrix because a thicker layer of oxides has formed and solid magnesium oxides are non-conductive. In SKPFM, a potential is applied to counter the electron flow as a result of equilibrating Fermi levels, but the bias potential cannot be applied to non-conductive materials. Zinc and aluminium showed and increased nobility due to the formation of oxides by increased Volta-Potentials [76, 77]. Therefore it is thought that this decreased potential surrounding secondary phase particle is due to the thickness of the magnesium oxides. To confirm this, SKPFM measurements should be conducted on thick magnesium oxide films or pure magnesium oxide.

The corrosion product was formed from the magnesium-based matrix and covered the surface from outside-in, therefore big particles were not yet fully covered and still showed a peak in potential in the middle. Even though the secondary phase particle was partly covered, the exposed area is still nobler than the surface. The potential of the centre were 490 and 580 mV which is a shift to a higher potential. The presence of a peak in potential in the middle was seen often, but a shift to a more noble potential was not. It is not sure why the potential shifted in this experiment. Cathodic centres were seen during immersion of WE43 in SBF by Kalb *et al.* [78], consisting of zirconium- and iron-rich precipitates. They saw volcano-shaped structures (circular areas surrounding cathodic centres) of magnesium hydroxide grow within the first minutes of immersion. After one second of immersion, dark spots became visible. After 2 hours of corrosion, a layer covered the cathodic centres. The volcano-shaped structure protected the precipitate from corrosion while bulk degradation took place. These reported volcanic structures surrounding precipitates and the precipitates were bigger than in Mg-4Zn, though the covering mechanism of the particle might be similar. The peak in potential surrounded by a negative potential seen at approximately (35,9) µm and (20,40) µm, might a small volcano-shaped structure. When looking at the smaller particle at approximately (25,45), there is no increased potential in the middle of the particle and thus is probably fully covered by corrosion products.

Volta-potential maps were also taken after immersion in water. In the maps presented in Figure 3.9, a grain boundary triple junction on a corroded surface by 4.75 hours of immersion in water can be seen clearly. The secondary phase particle at (25,8) shows a lower potential and an increased height of 275 nm compared to the matrix. A layer of corrosion product is again formed on and around the secondary phase particle with a lower potential. The disappearance of the peak in potential indicates that the second phase particle was fully covered by corrosion products after

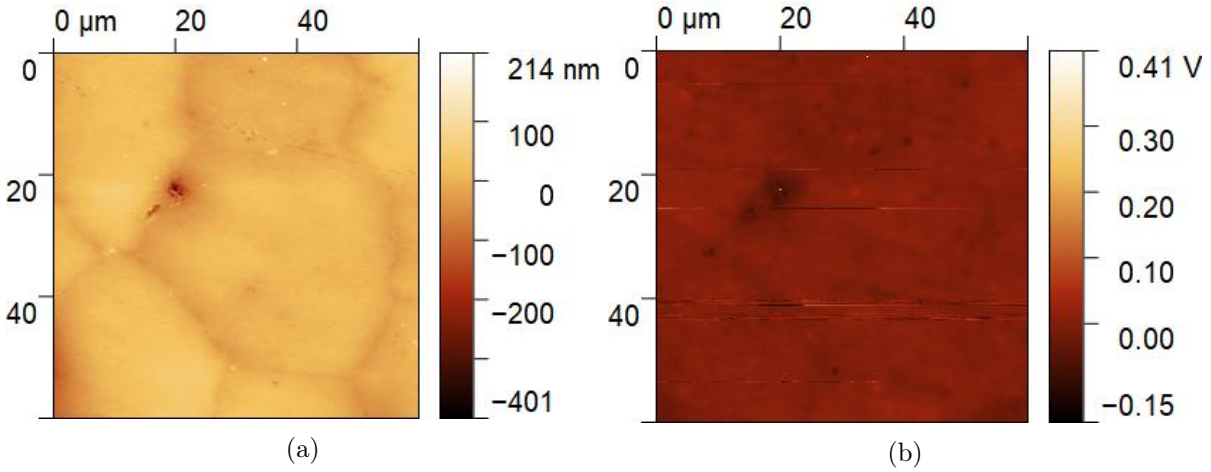

Figure 3.10: SKPFM result showing a topographical map (a) and a Volta-potential (b) showing a void in the grain boundary of a Mg-4Zn scaffold.

immersion. Due to the immersion in water, this sample was more corroded than the previously described corroded sample by over-polishing. The average potential in the grain (on the lower right 15 by 15 µm corner) is 9 ± 7 mV, which is higher than the previously measured potentials of -0.5uV for pure magnesium but in the same order of magnitude for the non-corroded and slightly corroded magnesium-based matrix in Mg-4Zn of 3 ± 10 mV and 9 ± 7 mV respectively. The small elevation in the potential of the matrix shows that a thin layer of corrosion product has formed on the surface, which is nobler than the bare magnesium-based matrix.

3.3.3 Implications of the Volta-potential to the corrosion behaviour

The Volta-potential map in Figure 3.7b showed that the precipitated secondary phase particles have a 140 mV higher potential compared to the magnesium-based matrix. With such a high difference, galvanic coupling will most likely occur, decreasing its corrosion resistance, as compared to pure magnesium. However, the opposite holds true; after 28 days of immersion, the scaffolds are less corroded than pure magnesium. The size and volume fraction of the precipitates play an important role in the propagation of galvanic corrosion. The particles are relatively small, therefore they get covered easily by corrosion products and the diffusion of bulk solution onto the surface is blocked. Contact between the two phases is needed in addition to contact with an electrolyte. By blocking the contact, corrosion cannot occur.

Another effect of the particles' small size is that the area with which they are adhered to the matrix is small. Therefore, the particles can be removed or fall off by mechanical force. This is seen in Figure 3.10 where a sample was sanded and polished twice. Polishing for 30 seconds to a minute was generally enough after thorough sanding with 4000 grit sandpaper. Here, it was sanded with 1200 grit and polished with great force until the surface appeared to be smooth. Polishing liquid could corrode the surface as was seen before. But by applying an appreciable amount of force, the corrosion products can be removed. Polishing affected the matrix notably more than the secondary phase particle. The matrix got polished away and the secondary phase particle was left exposed, the mechanical force of polishing then removed the particle from the interface between the grains and left a small void. The void at (20,20) µm in Figure 3.10a indicates the past position of the secondary phase particle. A drop in potential in Figure 3.10b accompanies this void.If the secondary phase particle detaches from the matrix, its contribution to galvanic coupling and thus corrosion, is eliminated.

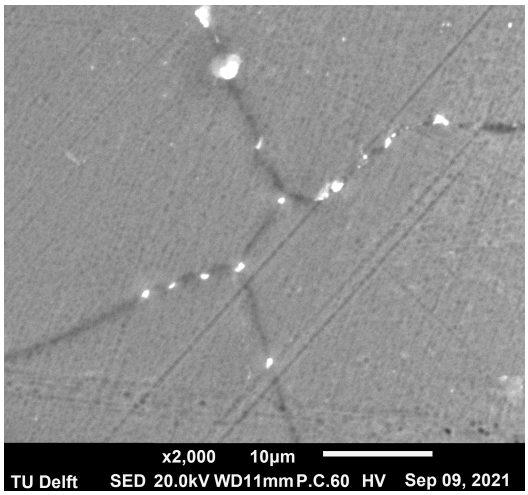

Figure 3.11: SEM image showing secondary phases particles on a corroded surface of a Mg-4Zn scaffold, after 4.75 hours of immersion in water at 2000x magnification.

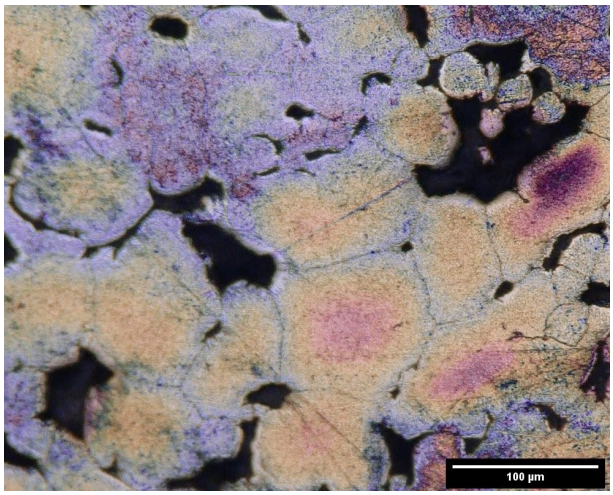

Figure 3.12: Optical microscopy image of a Mg-4Zn corroded surface after 4.75 of immersion in water at 1000x magnification.

Immersion tests were carried out in stagnant water only. The secondary phases were still present after immersion. Secondary phase particles can be seen in SEM images after immersion in stagnant water in Figure 3.11. The effect of dynamic fluids, such as flowing blood plasma in the body, might detach the secondary phase particle as was seen by the detaching of the particle with mechanical force.

In Figure 3.12, a scaffold after 2 hours of immersion in water is shown where there are different colours towards the grain boundaries than at the centre of the grains. The colour difference is most likely due to the different thicknesses of the oxide phase as also seen in anodised titanium and aluminium. The colours towards high wavelengths are observed for thicker oxide films [79]. The edges of the grains in Figure 3.12 have colours corresponding to the higher wavelengths (violet, blue and green), whilst the centre of the grain show colours corresponding to the lower wavelengths (red, orange and yellow) in the colour spectrum. The oxide layer at the grain edges are thus thicker than the centre, and corrosion starts from the grain boundaries. Smaller grains, as can be seen in the upper left corner in Figure 3.12, are almost homogeneously coloured blue and thus almost homogeneously covered by MgO. Magnesium alloys with fine grains are more susceptible to corrosion than coarse-grained magnesium alloys as IGC is more severe [80].

The secondary phase particles are mainly precipitated around the grain boundaries and thus dominate the corrosion around the grain boundaries only. Grain boundaries are already corrosion initiation sites, therefore the location of initiation sites are not affected by the presence of the particles. But the IGC is accelerated by micro-galvanic corrosion. The accumulation of secondary phase particles around the grain boundaries could be minimised by heat treatments. The secondary phases can be dispersed through T6 heat treatment or dissolved in the matrix using T4 heat treatment [40]. Heat treatments could thus increase the corrosion resistance of the alloy, which can be a subject for further research.

The secondary phase particles are of sizes of only a few hundred nanometers, but the particles' presence is enough to start micro-galvanic coupling. If the cathode (the secondary phase particles) is bigger than the anode (the matrix), the anode is violently attacked. But when the anode is bigger than the cathode, there is no significant attack of the anode and low galvanic corrosion is

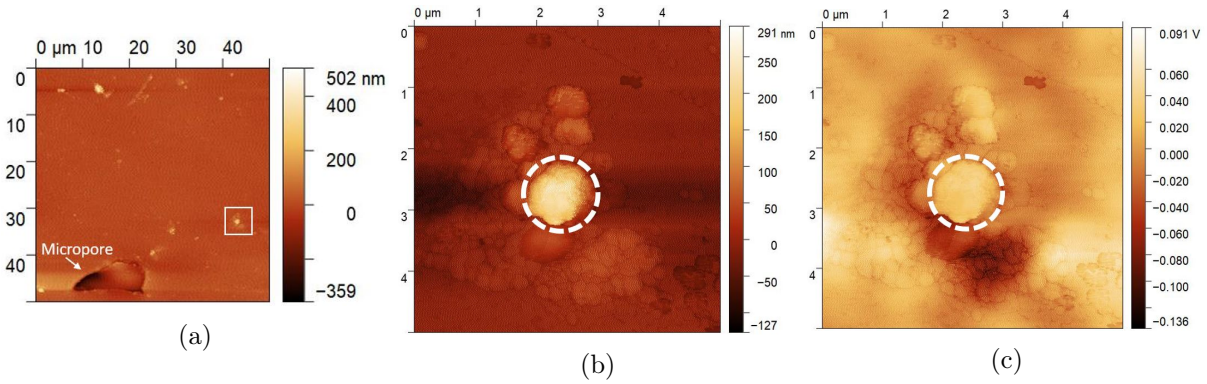

Figure 3.13: SKPFM result showing a topographical map of a polished Mg-4Zn scaffold (a). The white squares indicate the areas measured in (b) the topography map and (c) the potential map with the white circle indicating the edges of a secondary phase particle.

seen generally. This is presumably the case of the Mg-4Zn alloy, where only 4 weight percentage is zinc, and the secondary phase particles are on average less than a micron. But corrosion is still, however, inevitable.

All scaffolds were sanded and polished to expose the secondary phase particles. But when these scaffolds are applied to the body, they will be used as printed. Most secondary phase particles will thus not be exposed to blood plasma and cause micro-galvanic corrosion. Only when the scaffold is corroding, the particles will become in contact with water and thus their role as local cathodes are postponed until they are uncovered as the matrix corrodes away. In addition to the possibility of being covered by corrosion products or detached from the scaffold, their effect is considered to be less destructive than micropores.

The topography and Volta-potential maps shown before are measured over an area of approximately 2500 µm^2 (50 by 50 µm) and 256 measurements per line (pixels). SKPFM is a powerful technique used to characterise the corrosion processes associated with local features on a surface with a high resolution. This high resolution is a great advantage and in this thesis, the SKPFM was not used to its fullest potential. For the maps, an area of 2500 µm^2 was chosen, to investigate a whole grain and the precipitates around the grain boundaries. The maps in Figures 3.13b and c are measured over a 25 µm^2 (5 by 5 µm) area with 512 measurements per line, yielding a much higher resolution. In Figure 3.13c a secondary phase particle can be seen surrounded by an area of lower potential which confirms that the secondary phase possesses higher nobility than the area surrounding the particle. The secondary phase particle can be seen with above and below some haze with either higher or lower potential. The haze with higher potential might be secondary phase particles that were beginning to precipitate, cross-sections of secondary phases which were not cut through in the middle, smeared out secondary phase particles residue or corrosion products however this cannot be said with certainty.

3.4 The influence of micropores on the corrosion of porous scaffolds

The influence of morphology on the corrosion of porous scaffolds was determined by *in vitro* SECM measurements. In preparation for the measurements, two standard procedures were employed; recording a cyclic voltammogram and measuring an approach curve towards the substrate. Cyclic voltammetry was performed in r-SBF to determine the steady-state diffusion-controlled limiting current, which can be measured as a result of the oxidation reaction of ferrocenemethanol. The steady-state limiting current is the highest measured current in cyclic voltammetry.

Cyclic voltammetry was also performed to examine whether the tip was contaminated or damaged. The cyclic voltammograms were taken far above the surface to ensure there was no influence of the surface. The cyclic voltammograms from 0 to 0.5 V and from -1 to 1 V, can be found in Figure 3.14a and 3.14b respectively. The limiting current in 0.5mM Ferrocenemethanol/ r-SBF was around 2.5 nA. Lower current values such as 2.3 nA and 0.8-1.6 nA were also measured, however in this latter case, the low limiting current indicated a contaminated tip.

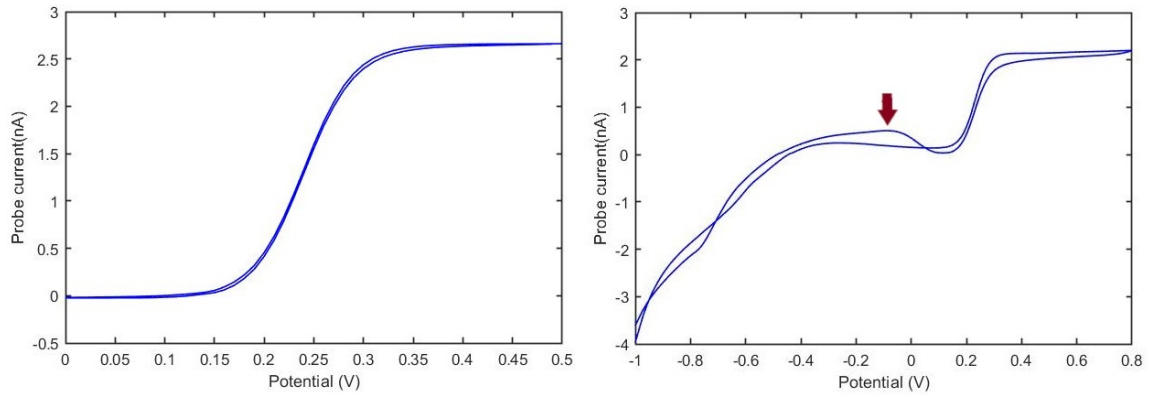

(a) (b)

Figure 3.14: Cyclic voltammograms from (a) 0 to 0.5 V and (b) -1 to 1 V recorded in r-SBF/0.5 mM ferrocenemethanol measured with a scan rate of 10 mV/s. A local maximum can be seen at -0.1 V, which corresponds to hydrogen evolution.

Approach curves towards the substrate were taken to determine the distance between the UME and the substrate, in order to position the tip of the UME at a known distance above the surface. This distance is important as a small distance between the substrate and the tip can block the diffusion of ferrocenemethanol. And a high distance will lead to the UME not being able to measure local features, or at an exceptionally high distance, the UME will not be influenced by the substrate in any case. Approach curves were taken directly on the strut, on epoxy resin or on the tape that covered the surface. In the latter case, the tip was lowered an additional height corresponding to the thickness of the tape (40 µm).

Since the M370 program could be set to lower the tip and automatically stop at a reduced current of 88% of the bulk current, an approach curve at a high velocity could be achieved. Figure 3.15 shows two approach curves taken from approximately 1500 µm (figure 3.15a) and 450 µm (figure 3.15b) from the surface of the resin and tape respectively. The approach curve in Figure 3.15a was taken at a higher distance from the surface. Therefore, the UME was lowered faster at 20 µm/point and 50 µm step and sweep velocity, compared to the approach curve in Figure 3.15b which was taken closer to the surface at 10 µm/point and 20 µm step and sweep velocity.

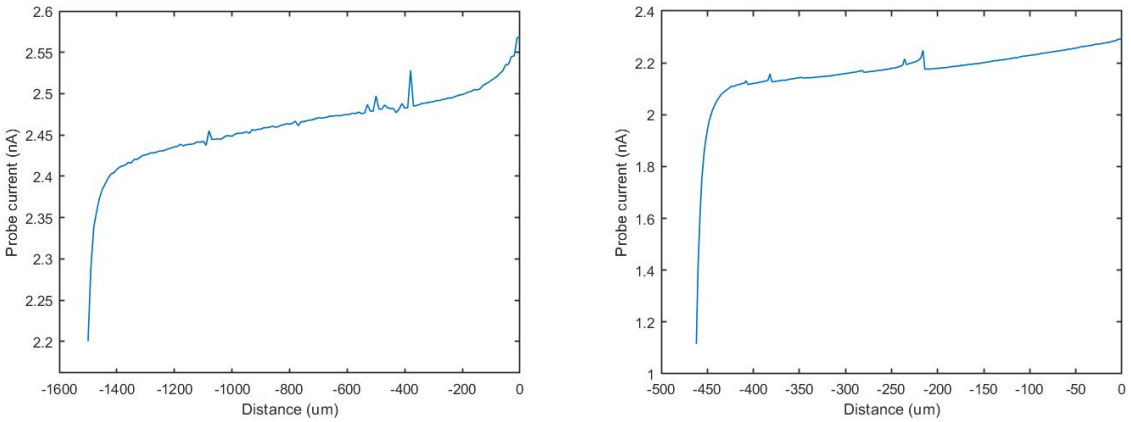

(a) (b)

Figure 3.15: Approach curves at (a) -2000 µm, 20 µm/point, 50 µm/s on resin, and (b) -500 µm, 10 µm/point, 20 µm/s measured on tape at an applied bias of 0.5V.

Approach curves made directly on the strut while being exposed to the r-SBF experienced trouble as hydrogen bubbles covered the surface. The bubbles could be stuck on the UME tip and impede the measurement. Bubble formation can be seen in Figure 3.16 after 2, 5 and 20 minutes of immersion. These bubbles form at the surface but will eventually detach from the surface. In Figure 3.16c, bubbles are located mostly at the intersections of the struts, giving rise to bubbles spaced out at a set distance. The scaffolds were set in epoxy resin, but due to shrinkage during curing, the scaffolds are not fully enclosed by the epoxy resin, causing a small gap between the epoxy resin and the strut where liquid can seep in and corrode the scaffold. At the interface between perpendicular struts, there is more area exposed to r-SBF thus more hydrogen bubbles are formed.

This vigorous hydrogen evolution in the form of hydrogen bubbles did not allow a stable approach curve to be measured on top of the bare strut, since the bubble led to noise. In addition, if the tip approaches hydrogen gas, there is an absence of ferrocenemethanol and thus a drop in current is measured which terminated the approach. Therefore approach curves had to be taken on epoxy resin next to the struts, or on the tape covering the strut for a stable approach curve. In Figure 3.17 approach curves made on the tape, strut and resin are shown where disturbances in the approach curves on strut are visible. These approach curves are of different lengths as they were made in different experiments. It shows the clear difference between a stable approach on resin and tape and an unstable approach on the strut. Using tape to cover the surface had the

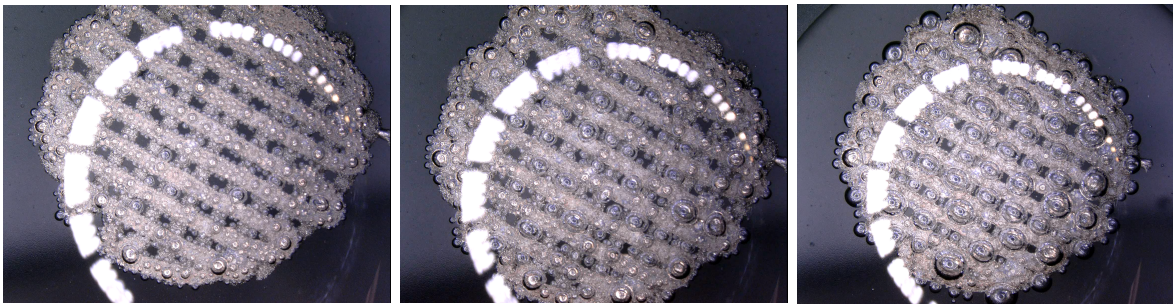

(a) (b) (c)

Figure 3.16: Mg-4Zn scaffold after (a) 2, (b) 5, and (c) 20 minutes of immersion in r-SBF at room temperature. The white ring is light from the microscope reflected from the surface.

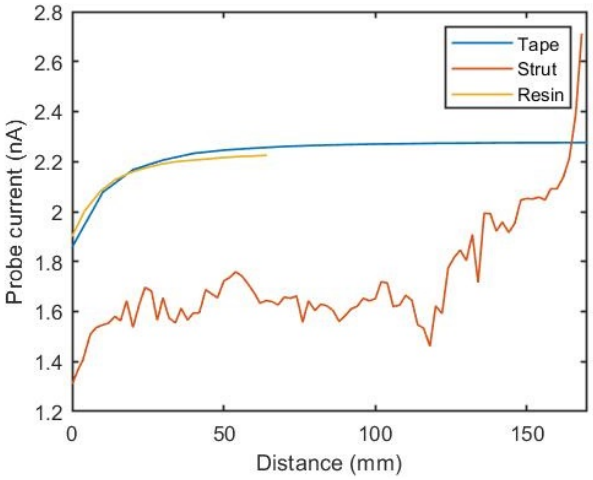

Figure 3.17: Approach curves measured on (a) tape, (b) strut and (c) resin. The approach curves measured in tape and resin are stable. The approach curve made directly on the strut shows disturbances by hydrogen formation.

advantage of protection of the surface from water and electrolyte while making approach curves, but tape removal could tilt the sample slightly. Approach curves show a straight part related to the limiting current under best circumstances, as can be seen in the approach curve made on the tape in Figure 3.17. But most of the time, a small slope was measured, as can be seen in Figure 3.15a, where the slope is 0.1 nA over a 1500 µm distance. The slope is a result of the depletion of the redox mediator due to the size of the tip. This slope of 0.1 nA over 1500 µm is very small and does not affect the approach curve quality.

After the approach curves and cyclic voltammetry, the tip was placed 20 µm above the surface for line scans. The samples were mounted with the struts in a vertical direction while line scans were taken in the horizontal direction after an undefined amount of time over a distance of 2500 µm or lower. In Figure 3.18a there are clear distinctions between resin and strut as the measured current measured at -0.1 V for hydrogen goes to zero almost every 400 µm. The sample measured here had a strut size of 420 ± 60 µm and a micropore size of 330 ± 40 µm. The standard deviation of the measured strut and macropore sizes is considerably large. Therefore, the blue blocks in Figure 3.18 might not correspond perfectly to the true macropore sizes.

This clear distinction of struts and macropore were only seen at hydrogen potential, but not clearly seen in the current measured at the potential for ferrocenemethanol, see Figure 3.18b. Hydrogen is formed on the surface of the struts, while epoxy resin does not produce hydrogen. The concentration of hydrogen on the epoxy resin does increase over time as the produced hydrogen gets dissolved in the bulk solution. The small difference in currents measured for ferrocenemethanol between the epoxy resin and the struts are because the samples are sanded and polished as described in the experimental section and are thus relatively flat in the early stages of immersion. The height differences at the edges of micropores are seen well, due to the volumetric contraction of epoxy resin during curing, therefore the resin is not fully filling the macropores. Great height differences were not expected between strut and resin in the early stages of immersion.

A closer look was taken at small sections of measured currents. There were two types of ferrocenemethanol current progressions measured over time; an increase or decrease. An increase is seen from 300 to 500 µm, while a decrease is seen from 1200 to 1400 µm and 1900 to 2300 µm. The increase and decrease of current can develop interchangeably as can be seen between 1200

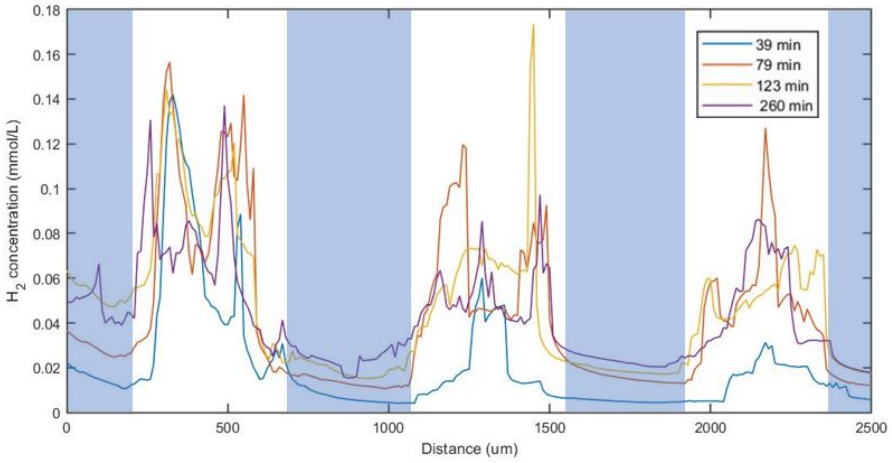

(a)

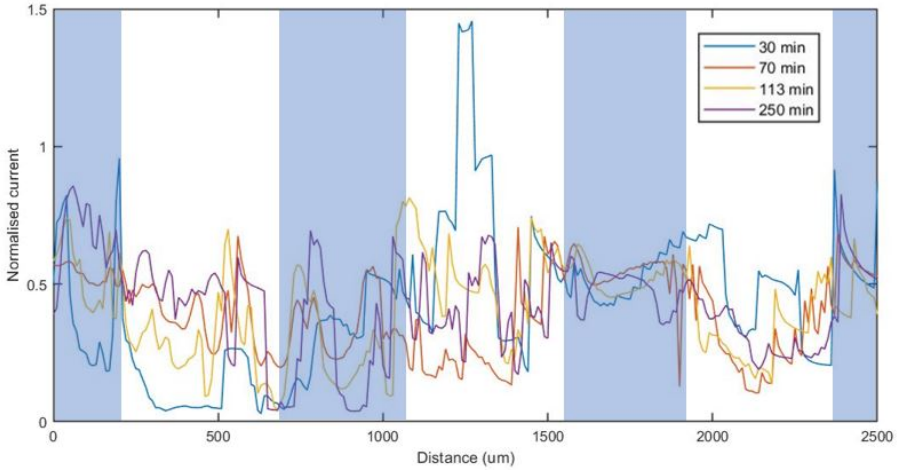

(b)

Figure 3.18: SECM plots of (a) hydrogen and (b) ferrocenemethanol measured on a Mg-4Zn scaffold in 0.5mM ferrocenemethanol/r-SBF solution at different immersion times. Blue blocks indicate the resin of 330 ± 40 µm, the exposed scaffolds are 420 ± 60 µm.

and 1500 µm in Figure 3.18b, where the current first increases then decreases.

3.4.1 The effect of surface morphology at a decreasing surface height

In Figure 3.19 the part from 250 to 550 µm from Figure 3.18 is shown. The normalised current for ferrocenemethanol shows an increase over time, which corresponds to surface dissolution. At 30 minutes, the surface is relatively flat between 300 and 500 µm, but there is some small surface roughness at 300 to 350 µm. At 39 minutes, the measured hydrogen current shows a local maximum at 325 µm. This verifies that surface roughness correlates with increased hydrogen production. The formed peaks could also be due to micropores as a result of the shrinkage of epoxy resin. At a micropore edge, an increased area was exposed to the solution and more hydrogen is produced in that small area. But the ferrocenemethanol showed a local increase in depth thus it is likely that a pit is formed. After 113 minutes small pits are formed on the surface, indicated by the peaks in Figure 3.19b at 300, 350 and 450 µm. At 300 to 350 µm surface roughness was seen, which had developed into a pit. This surface roughness was thought to be a micropore, which became a pit initiation site. The peaks at 450 µm however, were formed

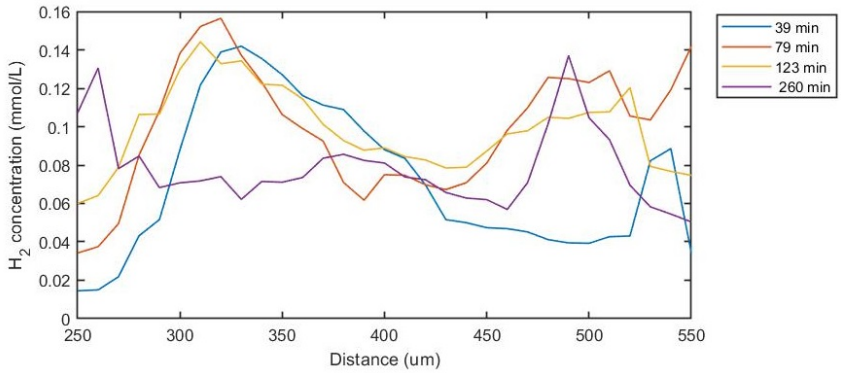

(a)

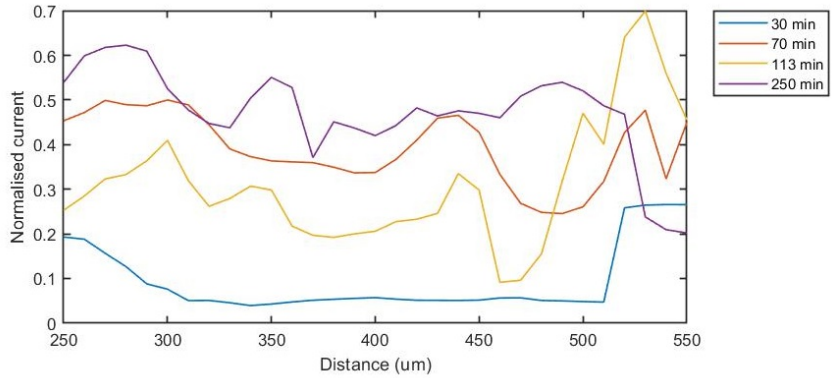

(b)

Figure 3.19: SECM plots of (a) hydrogen and (b) ferrocenemethanol from 250 to 550 µm from Figure 3.18.

on a surface that was flat before. The formation of peaks from a flat surface is due to pitting corrosion. As said before, the surface was sanded and polished, resulting in a flat surface and the sample was only immersed for 30 minutes. Therefore it cannot be said with certainty if there was a micropore or a flat surface before immersion. Nevertheless, these formed peaks in surface height are evidence of pitting corrosion.

Between 70 and 113 minutes of immersion, the surface became higher and the pores became less deep. The heightening of the surface is due to magnesium hydroxide forming on the surface and precipitation of phosphor- and calcium-containing products. Between 113 and 250 minutes, the pits at 300 and 350 µm became wider and deeper. After 260 minutes, there is no peak in hydrogen formation at 300 µm, this indicates that the pitting has slowed down. The pit seen at 450 µm at 113 minutes of immersion has flattened out, as the peak is absent after 250 minutes of immersion. The levelling out of the surface is either due to protection of the surface by a corrosion layer or an attack around the pores. The latter is unlikely as it was proven that pitting corrosion is occurring.

Pitting corrosion is a major contributor to the corrosion of pure magnesium scaffolds [42]. It was found that Mg–5Zn alloy with Mg_xZn_y and impurity secondary phase particles, shows severe corrosion along the grain boundaries. The magnesium matrix around the secondary phases suffered a severe attack and corrosion pits. The matrix was preferentially corroded due to corrosion acceleration caused by micro-galvanic corrosion. But after 24 hours of immersion, the Mg-5Zn alloy was uniformly corroded with no deep corrosion pits [41]. The blocking of pitting corrosion was also seen after 106 minutes in Figure 3.20. At 150 and 300 µm a peak was formed

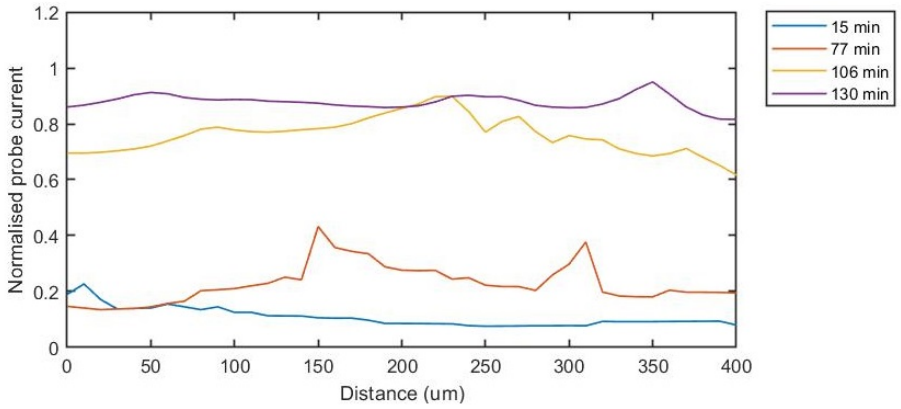

Figure 3.20: SECM plots of ferrocenemethanol after 15, 77, 108 and 130 minutes of immersion.

after 77 minutes which was not measured at 15 minutes. This is evidence of pitting corrosion occurring at a location that was flat. But after 130 minutes, the surface has flattened. These local maxima are flattening with an increasing amount of time, due to levelling out of the surface. The pit depth are decreased as the corrosion layer that covers the surface of the pits, protects the underlying surface from fast preferential attack.

After immersion, the surface was analysed with EDS. All surfaces identified with EDS after corrosion were not gold-sputtered. Pores were more difficult to differentiate from the matrix, compared to before immersion, as seen in Figure 3.2. On the EDS measurement in point 2 in Figure 3.21, an area assessed to be a micropore is filled and covered by magnesium oxide. In point 1 calcium, phosphor, carbon and sodium are also measured additionally to magnesium and oxide, which shows that the corrosion layer is complex as it consists of multiple products. Magnesium oxide results from the drying of magnesium hydroxide. This confirms that the pores are filled with corrosion products which can flatten out the surface as seen at 450 µm in Figure 3.19b. The inhomogeneous surface topography evens out as time progresses. This can be seen as the measured current shows less extreme local maxima and minima in Figure 3.18b.

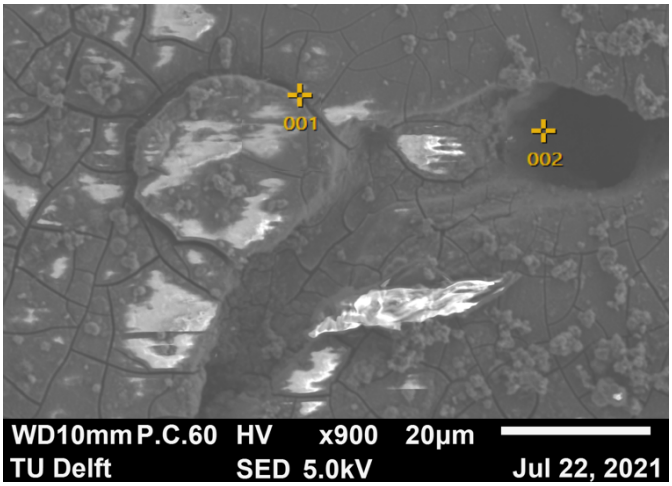

(a)

	P	O	C	Na	Mg	Ca
001	12.51	47.60	5.81	1.77	12.53	19.79
002		23.51			76.49	

(b)

Figure 3.21: SEM image (a) and corresponding EDS results in weight percentage (b) of Mg-4Zn scaffold after 3.5 hours of immersion in r-SBF at room temperature.

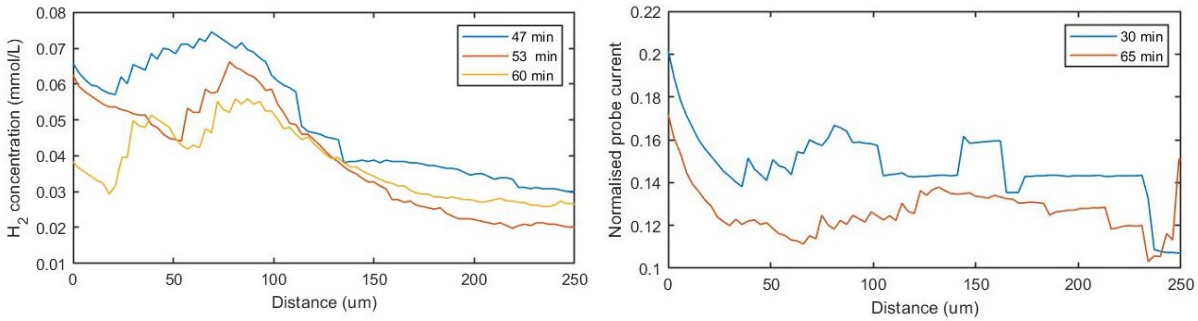

(a) (b)

Figure 3.22: SECM plots of (a) ferrocenemethanol and (b) hydrogen measured on a Mg-4Zn scaffold in 0.5mM ferrocenemethanol/r-SBF solution at different immersion times.

The average measured current increased, indicating that the distance between the tip and the surface decreased. The increase in distance from the surface reveals that the surface is being dissolved, faster than corrosion products precipitate. The magnesium hydroxide formed on the surface would protect the underlying magnesium to a certain extent. The magnesium hydroxide is porous and the solution can penetrate through the pores. Chloride reacts with magnesium hydroxide and forming magnesium chloride which can be dissolved, thus further decreasing the protective ability of magnesium hydroxide. At the same time, other corrosion products can precipitate onto the surface. Calcium phosphates were the main constituents. The average current can also decrease, indicating deposition of corrosion products.

3.4.2 The effect of surface morphology at an increasing surface height

This decrease in current was observed from 1200 to 1400 µm and 1900 to 2300 µm in Figure 3.18b. In another measurement with a step size of 2.5 µm, thus a higher resolution, the decrease in current was also detected. A line scan for hydrogen was carried out preceding this measurement to identify a strut. Then the step size was reduced. A smaller scanning distance was chosen to reduce the duration of the measurement. In Figure 3.22b, an overall decrease of normalised current is observed after 65 minutes, accompanied by a decrease of hydrogen concentration after 60 minutes. The flattening of the measured current indicates that the height between the tip and the current decreases, most likely due to the precipitation of corrosion products on the surface. From approximately 40 to 100 µm, a very rough surface can be seen in Figure 3.22b, which translates into increased hydrogen production at the same location as shown in 3.22a. The rough surface became less rough between 30 and 65 minutes of immersion and the peak at 150 µm disappears.

The dissolution of the surface and the formation of a protective corrosion layer are simultaneous events. However, precipitation of white corrosion products was only observed locally. In Figure 3.23, the surface of a sample after being immersed in water for 4.75 hours and after 4.5 hours immersion in 0.5 mM ferrocenemethanol/r-SBF are seen. The sample was set in epoxy resin with a tilt, so both horizontal and vertical struts are observed. The main difference is the precipitation of white corrosion products on the surface when the sample is immersed in r-SBF. Another difference is the size of pores on the scaffold; larger pits are seen on the surface corroded by r-SBF than on the surface corroded by water. This is attributed to the presence of chloride.

It is suggested that the maps in Figure 3.22 are made from a location where the white corrosion products have precipitated, protected the surface and gave rise to low hydrogen current measured

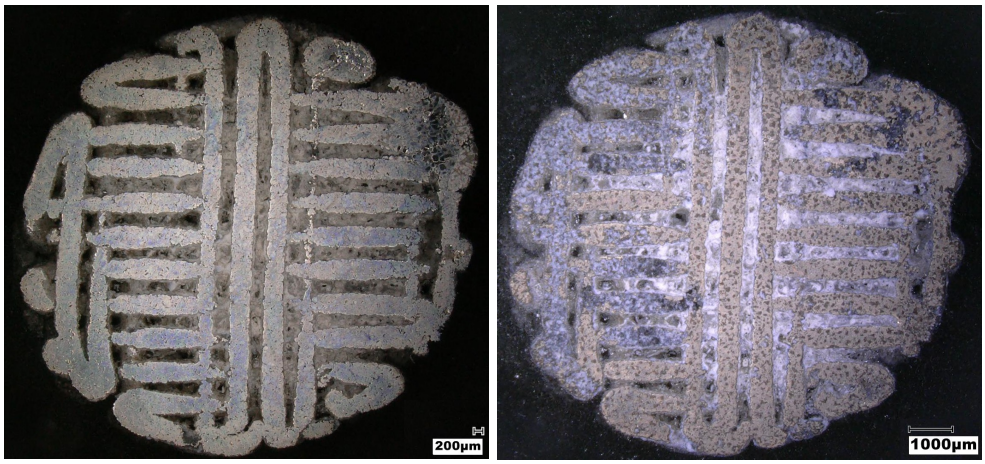

(a) (b)

Figure 3.23: Cross-section of a Mg-4Zn surface immersed in (a) water for 4.5 hours and (b) 0.5mM ferrocenemethanol/r-SBF for 4.75 hours.

after 60 minutes of immersion. The measured hydrogen concentration in Figure 3.22 is ≈ 0.5 mmol/L and the value decreases. The measured hydrogen concentration in Figure 3.19a is (≈ 1 mmol/L) and this value increases. The amount of produced hydrogen increased as the surface height decreased, while the amount decreased as the surface height increased. This confirms that the precipitation of corrosion products protects the underlying surface from corrosion.

3.4.3 The advantages and limitations of the SECM

The SECM has been shown to be a powerful technique allowing *in situ* and *in vitro* immersion tests, to monitor localised corrosion processes with high spatial and electrochemical resolution. The immersion test and the SECM experiments were performed at room temperature, while the temperature is 37°C in the human body. Immersion at an elevated temperature would increase chemical activity and therefore corrosion resistance would be lower. Although the use of a thermostatic bath could introduce noise to measured signals, performing SECM measurements at body temperature are desired, since it simulates the application in the body more closely.

SECM was used to map localised corrosion processes by scanning over a 1D line, as shown in section 3.4 but it can also be used to scan multiple lines to form an area map. The obtained map is then used to compare it with a microscopy technique such as an optical microscope or SEM. Maps such as those in Figure 3.24 could be obtained, where morphological components and hydrogen production can be correlated. It should be noted that at (50,-30) in the hydrogen map the Faraday cage was opened to check whether a hydrogen bubble was stuck on the surface, which was not the case.

The ferrocenemethanol map was measured first, using a step size of 5 µm which took half an hour, then the hydrogen map was measured using a step size of 10 µm. These maps were an exceptional case; all other SECM area measurements were comparable to Figure 3.25, where a gradient is seen between the bottom left and the top right due to increasing height by the formation of a corrosion layer. Obtaining a map of 250 by 200 µm with a step size of 5 µm took over 50 minutes and thus there is a 50-minute difference between the first and the last measurement. With a fast-changing surface, a long measuring time is not ideal. The map in Figure 3.24b was made using a step size of 10 µm, which was faster than 5 µm. But the average micropore size was approximately 10 µm, therefore the chance of moving over a micropore was high. There was also a great chance of tip contamination or a hydrogen bubble attaching to the

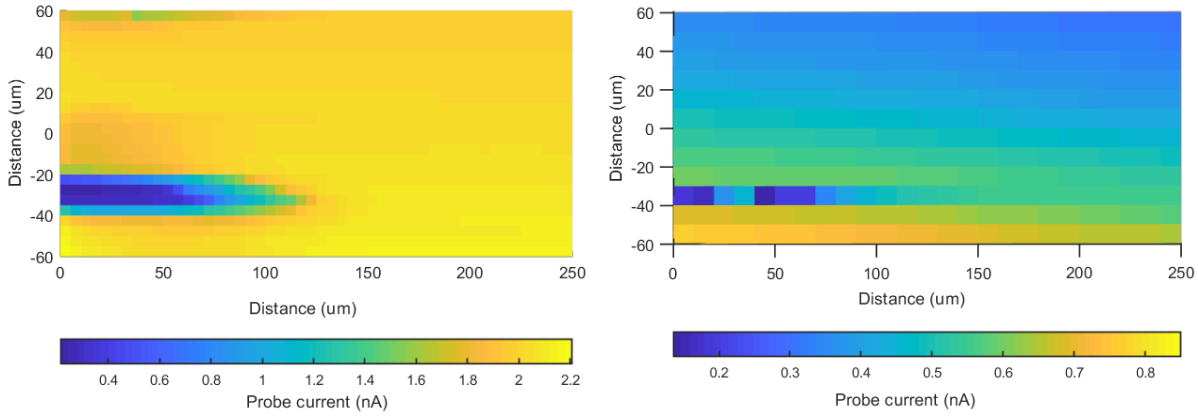

(a) (b)

Figure 3.24: SECM map of (a) ferrocenemethanol and (b) hydrogen during immersion in 0.5 mM ferrocenemethanol/r-SBF.

tip if the duration of the measurement was high. Therefore, it was decided that line scans would be more suitable for this system, where the tip could be raised between each line scan to remove possible bubbles attached to the tip. After a line scan, the UME would go to its origin with a velocity of 100 µm/s and shaking off a possible bubble.

A limitation of SECM in this thesis was the necessity of embedding the samples in epoxy resin. The resin is used to fix the scaffold in its position and as a support to create an electrochemical cell. The resin also served as filling to prevent polishing liquid from being trapped in the macro- and micropores and corrode them. But due to the epoxy resin, micropores are not fully exposed to the r-SBF. In addition, the fluids could be trapped between the epoxy resin and scaffold, thus creating a crevice that may not be present when applying the scaffold in the body. In addition, blood flows with a certain pressure through the scaffolds making crevice corrosion less likely. Therefore, the use of resin might have increased the crevice corrosion.

The focus of SECM was to determine the effect of micropores in immersion tests. A step size of 2.5 to 10 µm was used for SECM, which is bigger than the secondary phase size. The large step size was chosen to reduce duration of the measurement when scanning over a line of 2500 µm. This length was chosen as several areas of strut and macropores would be scanned. The effect of

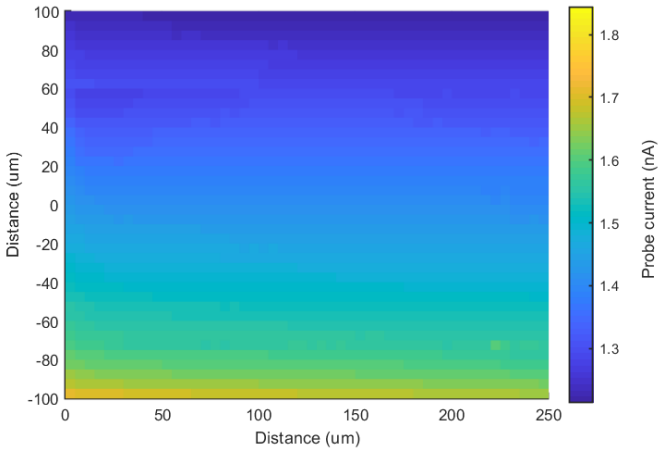

Figure 3.25: SECM map of ferrocenemethanol after one hour of immersion in 0.5 mM ferrocenemethanol/ r-SBF.

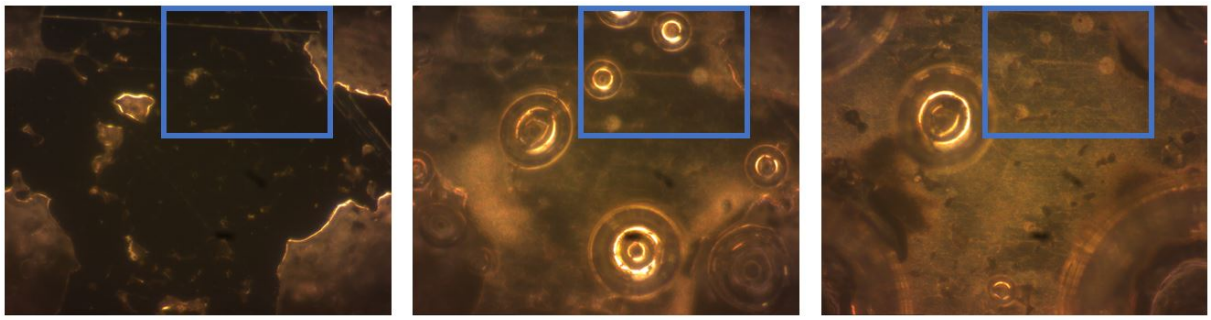

(a) (b) (c)

Figure 3.26: Mg-4Zn scaffold before (a) 2 and after (b) 6, and (c) 20 minutes of immersion in r-SBF at room temperature. The circular rings are bubbles of hydrogen gas formed on the surface. Nodules that are less severely attacked can be seen in the area marked by the blue rectangle.

secondary phase particles cannot be deducted with this step size and thus its effect on corrosion were not taken into account in section 3.4. If a smaller step size (0.5 µm) would be chosen, it might be able measure the effect of secondary phase particles. The SECM is known for its high resolution, however this system with perturbation caused by the generation of large quantities of hydrogen gas, is not ideal fro small step sizes. In addition, the secondary phase particles are slightly elevated compared to the surface, but as can be seen in Figure 3.18b, height differences between resin and pores are difficult to make, and the distinction of secondary phase particles would be unattainable.

Similar to Figure 3.16, a scaffold was sanded, polished and immersed in 0.5 mM ferrocenemethanol/ r-SBF under an optical microscope, but at a higher magnification. In Figure 3.26 lighter coloured nodules can be seen, with the sizes comparable to grains, which were less severely attacked. These nodules probably originate from the liquid sintering step, as heat can be inconsistently distributed. The area in Figure 3.26 is the intersection between two 0 and 90° struts. After 2 hours of immersion, the r-SBF was drained and the scaffold was dried. The surface was checked under optical microscopy, but the same location could not be found, see Figure 3.27. The nodules cannot be seen in SEM so its composition could not be analysed. These nodules could not be seen by eye and were also not seen with optical microscopy before immersion. Therefore, it is unknown if these nodules are regularly present or if these nodules were only formed in this sample only. In Figure 3.27, the lighter nodules can be seen but there is no severe attack around the nodules, which indicates that they are not more cathodic compared to the matrix.

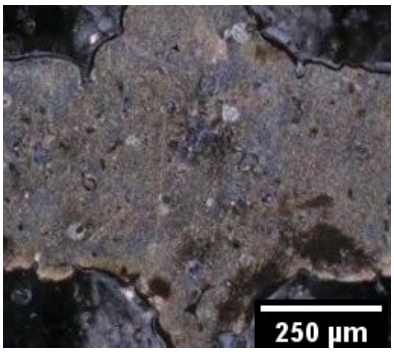

Figure 3.27: Cross-section of a Mg-4Zn scaffold after 2 hours of immersion in r-SBF at room temperature, with lighter coloured nodules.

3.5 Corrosion products

The term corrosion layer has been used to describe all generated species by contact between scaffold and air, water or electrolytes. The characterisation of the exact corrosion products was made using SEM, XRD and FTIR. The corrosion products from the reaction of magnesium with water and air were already given in section 1.2. Alternatively, magnesium hydroxide can also be formed, when oxygen reacts with magnesium [27]:

$$2\,Mg + O_2 + 2\,H_2O \longrightarrow Mg(OH)_2 \tag{3.1}$$

Magnesium hydroxide is formed regardless of which reaction occurs and is the main component in the corrosion layer. Magnesium hydroxide can dry and magnesium oxide is formed according to:

$$Mg(OH)_2 \longleftrightarrow MgO + H_2O \tag{3.2}$$

Magnesium cannot react directly with oxygen without high temperatures.

Up until now, the zinc degradation has been ignored as magnesium has a lower standard electrode potential. Meaning that magnesium becomes the anodic side of the galvanic cell when contact is made with zinc. Zinc can react in the same fashion as magnesium forming zinc hydroxide or zinc oxide:

$$Zn^{+} \longrightarrow Zn^{2+} + 2\,e^{-} \tag{3.3}$$

$$Zn^{2+} + 2\,OH^{-} \longrightarrow Zn(OH)_2 \tag{3.4}$$

$$Zn(OH)_2 \longleftrightarrow ZnO + H_2O \tag{3.5}$$

Alternatively, pure zinc can react with chloride forming $ZnCl_2$, zinc hydroxide carbonate and zinc hydroxide chloride[81]. Though, chloride will favour to react with magnesium hydroxide. The corrosion products of zinc are less susceptible to chloride attack, providing a more stable passivation layer than magnesium hydroxide. The composition of corrosion products was measured with EDS on corroded samples after 4.75 hours of immersion in water and after 4.5 hours of immersion in r-SBF.

In Figure 3.28a and c, the composition of the corrosion layer of a scaffold corroded in ultrapure water can be seen. The zinc content on the interior of the grain in area 5 is 8.9 wt.%. The area in the middle of the grain under the corrosion layer is a magnesium-based matrix. Therefore, the zinc content was expected to be lower than 4 wt.%. The measurements taken at points 1-4, were on secondary phase particles. Thus a higher zinc content is expected than the matrix. In points 1 and 3, this holds true, but in points 2 and 4 the zinc content is lower than the matrix. All measured points show values of zinc above 4 weight percentage. The increased zinc content indicates that the corrosion layer contains an increased amount of zinc compared to the uncorroded scaffold. An thus the corrosion products are stabler than the corrosion products of pure magnesium. This higher stability of the passive oxide film has been shown to reduce the corrosion rate [82].

In Figure 3.28b and d, the composition of the corrosion layer of a scaffold corroded after immersion in r-SBF for approximately the same duration as ultrapure water is seen. The zinc content is on average 2 wt.%, which is lower than the zinc content measured on the scaffold corroded by water. This decrease in is due to the additional calcium- and phosphorous precipitates. These precipitates protect the Mg-Zn surface from contact with the electrolyte, which reduces

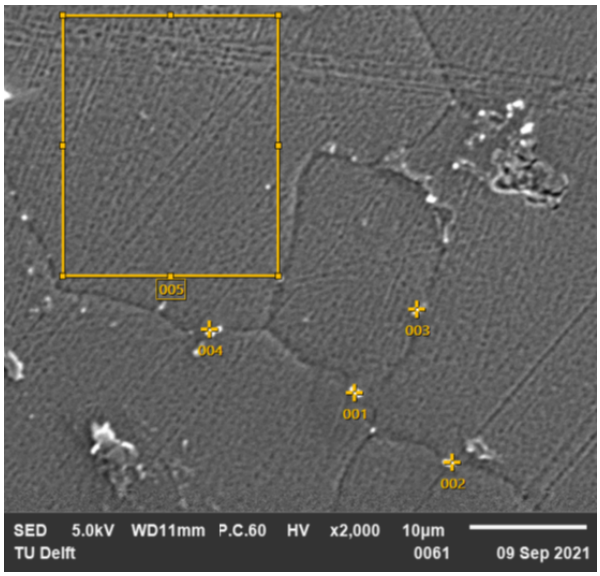

(a)

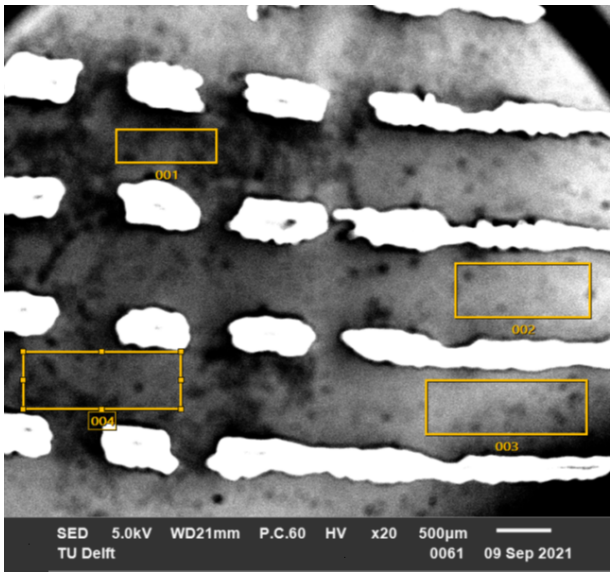

(b)

	O	C	Mg	Zn
001	44.93	9.66	32.05	13.36
002	47.67	7.81	38.51	6.00
003	31.96	5.34	44.27	18.44
004	46.12	7.58	38.15	8.14
005	47.84	9.90	33.40	8.86

(c)

	P	O	C	Na	Mg	Ca	Zn
001	13.77	40.48	6.03	1.70	20.21	16.41	1.41
002	7.06	26.34	6.43	1.72	39.16	16.12	3.18
003	7.85	26.68	5.89	2.83	37.72	19.03	
004	10.15	32.36	6.58	1.46	30.71	15.63	3.12

(d)

Figure 3.28: SEM images of Mg-4Zn scaffold after immersion at room temperature in water for 4.75 hours (a) and in r-SBF for 4.5 hours (b) with the corresponding EDS results ((c) and (d) respectively) in weight percentage.

the corrosion. The calcium to phosphor ratio in Figure 3.28b is approximately 1.2 to 2.4. This correlates to the Ca/P ratio of OCP (1.33), TCP (1.5) and hydroxyapatite (1.67). The Ca/P ratio was on the lower end of this spectrum determined during other measurements. Therefore the calcium-phosphorus compounds precipitated on the corroded surfaces will most likely be OCP or TCP and possibly DCPD (Ca/P=1), but not hydroxyapatite.

Two measured elements were not expected; carbon and sodium. In Figure 3.28a and c the presence of carbon is measured. This sample was corroded in ultrapure water, so there was an absence of carbon or carbonate. Carbon contaminants might have been present but an artificial carbon peak is always measured due to the high background counts. Another outstanding found element is sodium in 3.28b. Sodium is present in r-SBF but sodium-containing salts are highly soluble and therefore sodium was not expected to be found in the corrosion products. The overlapping X-ray emission peaks of sodium might be the reason. The Kα characteristic X-ray of sodium is at a similar energy as the Lα X-ray from zinc; 1.041 and 1.012 respectively. Therefore it is ambiguous whether sodium was present on the corrosion layer.

XRD diffraction was also performed on the corroded surface to characterise the corrosion products. The fraction of calcium-phosphorus compounds was too small to be detected compared to MgO. X-ray diffractograms of a polished and a corroded sample after 4.5 hours of immersion in r-SBF at room temperature can be found in Figures B.2a and B.2b in Appendix B. The diffractogram of the corroded sample shows a bump in the baseline between 25 and 40 degrees, which corresponds to calcium-phosphorous compounds. The bump does not show clear peaks, so the

characterisation of calcium-phosphorus compounds cannot be made using XRD.

The presence of phosphate ions (PO_4^-) was confirmed using Fourier-transform infrared spectroscopy (FTIR), see Figure 3.29 for the spectrum. The phosphates are most most likely in the form of ($CaPO_4^-$) as it has the highest equilibrium constant [69]. The FTIR spectrum shows O-H bonds which might be due to the presence of water but the O-H bond is also found in magnesium hydroxides and hydroxyapatite. Carbonates (CO_3^-) were as well found using FTIR, which explains the carbon found in the EDS measurements for scaffolds corroded in r-SBF. The carbonates are presumably originating from $MgCO_3$.

The corrosion products are identified, based on SEM, XRD and FTIR results. But in SEM, electrons can penetrate the surface more than the corrosion layer thickness. In addition, the quantity of light elements cannot be measured accurately. XRD cannot analyse small amounts and FTIR can only measure certain bonds. However, it can be concluded that the corrosion layer consists of calcium- and phosphate-containing corrosion products. The precipitation of these compounds protects the underlying surface. In addition, the incorporation of zinc-containing products in the corrosion layer increases the stability compared to the corrosion layer of pure magnesium, which exclusively consist of magnesium hydroxide. It is for this reason that the corrosion resistance of Mg-4Zn is better than pure magnesium, even though micro-galvanic coupling increases the corrosion rate.

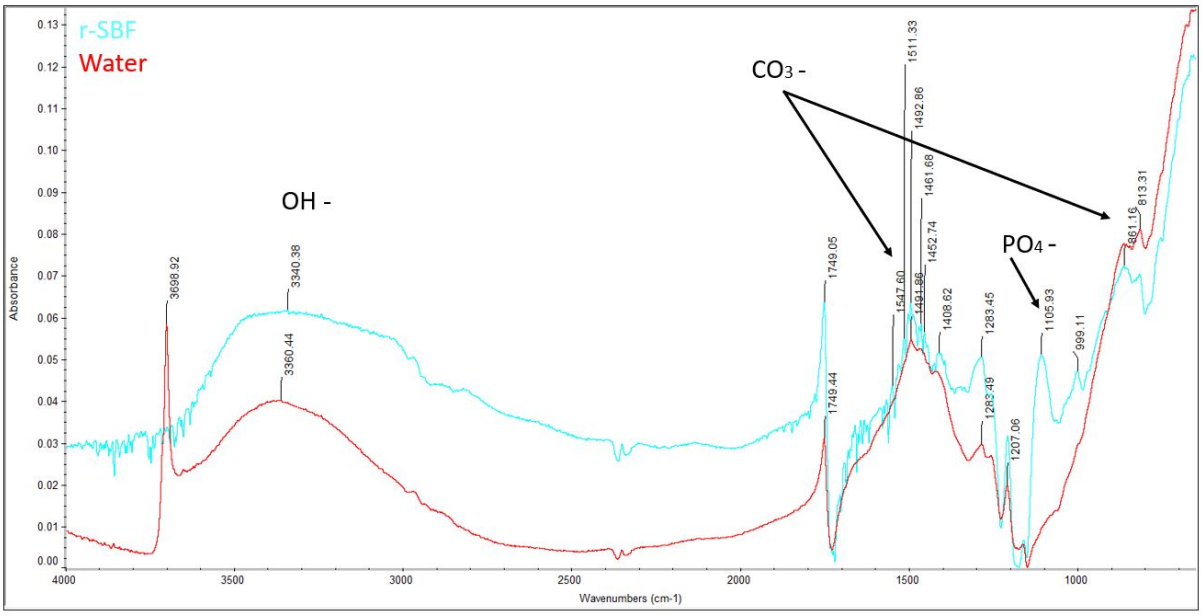

Figure 3.29: FTIR spectrum of Mg-4Zn scaffolds immersed for 4.75 hours in water and 4.5 hours r-SBF.

Chapter 4

Research recommendations

Based on this work, some future research recommendations were made in Chapter 3: Results and Discussion. Additional recommendations can be made to supplement the results on the effect of microstructure on the degradation of 3D printed porous Mg-4Zn scaffolds. SKPFM was used to analyse polished, etched and corroded surfaces. The corroded surfaces were immersed in water for 4.75 hours. Corroded surfaces as a result of immersion in r-SBF for the same duration were also scanned. The noise in these maps was very high as the corrosion products were not conductive. Immersion in r-SBF can be attempted for a less amount of time. In addition, water immersion can be attempted for a longer amount of time.

The solution used in SECM was r-SBF with 0.5 mM ferrocenemethanol. R-SBF is a complex solution due to all the different ions and it will attack the surface more than ultra-pure water due to the presence of chloride. For future research, water with 0.5 mM ferrocenemethanol can be used as a solution. This will reduce the number of bubbles since chloride attack will be eliminated. After water immersion, components of SBF can be added individually to test their individual contribution. Blood plasma mimicking solutions with proteins, such as albumin (the most abundant blood protein), can also be used in SECM. But these interactions between biomolecules and the metallic surface are much more complex than immersion in SBF. Immersion using proteins have been carried out for magnesium alloys [83–85], but not on 3D-printed Mg-4Zn scaffolds using SECM. All SECM measurements in this thesis were made at room temperature, but with the use of a small thermostatic bath, the temperature could be regulated to be 37°C. In addition, using a continuous flow of fluids could simulate the environment in the body more accurately than stagnant fluids. In this study, the immersion times were under 5 hours to investigate the initial reactions at micropores. It was found that the micropores can get filled with corrosion products within 130 minutes (in Figure 3.20), but they also could still be present after 250 minutes (in Figure 3.19b). Therefore, longer immersion times could be investigated as the scaffolds will stay in the body for weeks.

It has been stated before that the incorporation of micropores increases the surface to volume ratio and therefore decrease corrosion resistance. In this thesis, the scaffolds were set in epoxy resin and only stagnant fluids were used. To investigate the effect of increased area, immersion of 3D printed porous scaffolds can be compared with the immersion of the bulk counterpart in flowing fluids.

The exact composition and amounts of corrosion products were not measured with high accuracy. A technique that can be used to resolve this issue of the identification of the corrosion products, calcium-phosphorous compounds, in particular, could be X-ray photoelectron spectroscopy (XPS). Additionally, the corrosion layer thickness evolution could be followed by glow discharge optical emission spectroscopy (GDEOS).

Chapter 5

Conclusion

Additive manufacturing, or 3D printing, has made a significant impact on the manufacturing industry. It can produce complex structures in a fast and reproducible way. The innovation has also impacted biomaterials manufacturing. One such group of biomaterials are degradable biomaterials. The 3D printed porous degradable biomaterials provide support, whilst providing space for bone ingrowth. But there is a shortcoming in materials that can be 3D printed, are biodegradable and biocompatible. Magnesium can be used as a degradable biomaterial, but the corrosion resistance is not yet adequate. The addition of alloying elements changes the microstructure and thus its corrosion behaviour. It was found that the addition of 4 wt.% zinc increased the corrosion resistance. The effect of microstructure on the corrosion behaviour was analysed on extrusion-based 3D printed porous Mg-4Zn scaffolds, using localised electrochemical techniques.

The microstructure of extruded porous Mg-4Zn scaffolds consists of 25 ± 5 µm grains and secondary phase particles with a size of 0.6 ± 0.3 µm precipitated along the grain boundaries. The composition of secondary phase particles is $MgZn_2$ in a magnesium-based matrix. The size of the micropores on cross-sections ranges between 1 and 70 µm with an average of 14 ± 11 µm and they form an interconnected network. The struts of the scaffolds are approximately 450 µm and printed in a 0°/90°/0° lay-down pattern approximately 300 µm apart.

The effect of secondary phase particles was investigated using SKPFM. The particles showed a Volta-potential of +140 ± 50 mV compared to the matrix. The high difference in Volta-potential indicates micro-galvanic coupling between the secondary phase particles and the matrix, where the particles will act as micro-cathodes. The secondary phase particles precipitated mostly along the grain boundaries. As IGC occurs, the particles do not give rise to new corrosion initiation sites. The size of the particles plays an important role; they are small and are easily covered by corrosion products or detach from the surface, terminating the micro-galvanic coupling. In addition, the secondary phase particles are not in contact with an electrolyte until they are uncovered by the corrosion of the matrix. This postpones the effect of micro-galvanic corrosion. Therefore, its contribution to corrosion is considered less than micropores.

The effect of micropores was investigated using SECM with immersion in r-SBF. It was found that the surface of micropores shows a higher corrosion rate. However, this surface is covered by corrosion products, which protects the underlying material from corrosion. Pitting corrosion was observed using SECM, but the pits are like micropores, covered with corrosion products consisting of magnesium hydroxide, magnesium carbonates, zinc-, calcium- and phosphor-containing compounds. The precipitation of calcium-phosphorous compounds protects the surface from

contact with fluids and the presence of zinc contributes to a more stable passivation layer than solely magnesium hydroxide.

In conclusion, the addition of zinc caused micro-galvanic corrosion between secondary phase particles and the matrix, but its contribution to corrosion is low due to postponed or blocked contact with the electrolyte. The presence of micropores increase the surface exposed to electrolyte and the micropores are corrosion initiation sites. But the surface is covered by a stabler corrosion layer than the corrosion layer formed on pure magnesium due to the presence of zinc. Therefore, the corrosion resistance of extrusion-based 3D printed Mg-4Zn scaffolds is better than the corrosion resistance of extrusion-based 3D printed pure magnesium scaffolds.

Acknowledgements

With the end of this thesis comes the end of my journey as a masters student at TU Delft. I have learned a great deal in the last two years. And I have learned a lot of practical skills during this master thesis project. I would like to thank a few people whose input cannot be left unnoticed as the finishing of this thesis could not have happened without them.

First of all, I would like to thank Dr. Yaiza Gonzalez-Garcia for not only being an excellent supervisor and answering my many questions. But also for her commitment by literally joining me in the lab one day until the evening.

I also wish to thank Jiahui Dong for all the great supervision and the help with sample preparations. I wish her the best of luck with the finishing of her PhD track.

My gratitude goes to Sajjad Mousavi and dr. Aytac Yilmaz for the help they gave me with AFM and SKPFM measurements.

For the help with SECM measurements, I would like to thank Ziyu Li.

Lastly, I would like to thank dr. Jie Zhou for his valuable input to make the thesis as complete as possible.

References

1. Steenhuis, H.-J. & Pretorius, L. The additive manufacturing innovation: a range of implications. *Journal of Manufacturing Technology Management* (2017).
2. Roseti, L., Parisi, V., Petretta, M., Cavallo, C., Desando, G., Bartolotti, I. & Grigolo, B. Scaffolds for bone tissue engineering: state of the art and new perspectives. *Materials Science and Engineering: C* **78,** 1246–1262 (2017).
3. Williams, D. F. On the nature of biomaterials. *Biomaterials* **30,** 5897–5909 (2009).
4. Vasireddi, R. & Basu, B. Conceptual design of three-dimensional scaffolds of powder-based materials for bone tissue engineering applications. *Rapid Prototyping Journal* (2015).
5. Palmer, L. C., Newcomb, C. J., Kaltz, S. R., Spoerke, E. D. & Stupp, S. I. Biomimetic systems for hydroxyapatite mineralization inspired by bone and enamel. *Chemical reviews* **108,** 4754–4783 (2008).
6. Marcus, R., Feldman, D., Nelson, D. & Rosen, C. J. *Fundamentals of osteoporosis. 2009*
7. Gao, C., Wang, C., Jin, H., Wang, Z., Li, Z., Shi, C., Leng, Y., Yang, F., Liu, H. & Wang, J. Additive manufacturing technique-designed metallic porous implants for clinical application in orthopedics. *RSC advances* **8,** 25210–25227 (2018).
8. Haines, N. M., Lack, W. D., Seymour, R. B. & Bosse, M. J. Defining the lower limit of a "critical bone defect" in open diaphyseal tibial fractures. *Journal of orthopaedic trauma* **30,** e158–e163 (2016).
9. Geetha, M., Singh, A. K., Asokamani, R. & Gogia, A. K. Ti based biomaterials, the ultimate choice for orthopaedic implants–a review. *Progress in materials science* **54,** 397–425 (2009).
10. Williams, D. F. On the mechanisms of biocompatibility. *Biomaterials* **29,** 2941–2953 (2008).
11. Hutmacher, D. W. Scaffolds in tissue engineering bone and cartilage. *Biomaterials* **21,** 2529–2543 (2000).
12. Okazaki, Y. & Gotoh, E. Comparison of metal release from various metallic biomaterials in vitro. *Biomaterials* **26,** 11–21 (2005).
13. Erisken, C., Kalyon, D. M. & Wang, H. Functionally graded electrospun polycaprolactone and β-tricalcium phosphate nanocomposites for tissue engineering applications. *Biomaterials* **29,** 4065–4073 (2008).
14. Vormann, J. Magnesium: nutrition and metabolism. *Molecular aspects of medicine* **24,** 27–37 (2003).
15. Ku, C.-H., Pioletti, D. P., Browne, M. & Gregson, P. J. Effect of different Ti–6Al–4V surface treatments on osteoblasts behaviour. *Biomaterials* **23,** 1447–1454 (2002).
16. Abd El-Rahman, S. S. Neuropathology of aluminum toxicity in rats (glutamate and GABA impairment). *Pharmacological Research* **47,** 189–194 (2003).
17. Zheng, Y. F., Gu, X. N. & Witte, F. Biodegradable metals. *Materials Science and Engineering: R: Reports* **77,** 1–34 (2014).
18. Liu, M., Schmutz, P., Uggowitzer, P. J., Song, G. & Atrens, A. The influence of yttrium (Y) on the corrosion of Mg–Y binary alloys. *Corrosion Science* **52,** 3687–3701 (2010).

19. Hort, N., Huang, Y.-d., Fechner, D., Störmer, M., Blawert, C., Witte, F., Vogt, C., Drücker, H., Willumeit, R., Kainer, K., *et al.* Magnesium alloys as implant materials–Principles of property design for Mg–RE alloys. *Acta biomaterialia* **6,** 1714–1725 (2010).
20. Yang, L., Huang, Y., Peng, Q., Feyerabend, F., Kainer, K. U., Willumeit, R. & Hort, N. Mechanical and corrosion properties of binary Mg–Dy alloys for medical applications. *Materials Science and Engineering: B* **176,** 1827–1834 (2011).
21. Yang, W., Zhang, P., Liu, J. & Xue, Y. Effect of long-term intake of Y3+ in drinking water on gene expression in brains of rats. *Journal of Rare Earths* **24,** 369–373 (2006).
22. Li, Y., Wen, C., Mushahary, D., Sravanthi, R., Harishankar, N., Pande, G. & Hodgson, P. Mg–Zr–Sr alloys as biodegradable implant materials. *Acta biomaterialia* **8,** 3177–3188 (2012).
23. Avedesian, M. M., Baker, H., *et al. ASM specialty handbook: magnesium and magnesium alloys* (ASM international, 1999).
24. Clark, J. & Rhines, F. Central region of the Mg-Zn phase diagram. *JOM* **9,** 425–430 (1957).
25. Xin, Y., Hu, T. & Chu, P. In vitro studies of biomedical magnesium alloys in a simulated physiological environment: a review. *Acta biomaterialia* **7,** 1452–1459 (2011).
26. Li, Z., Gu, X., Lou, S. & Zheng, Y. The development of binary Mg–Ca alloys for use as biodegradable materials within bone. *Biomaterials* **29,** 1329–1344 (2008).
27. Wang, C., Mei, D., Wiese, G., Wang, L., Deng, M., Lamaka, S. V. & Zheludkevich, M. L. High rate oxygen reduction reaction during corrosion of ultra-high-purity magnesium. *npj Materials Degradation* **4,** 1–5 (2020).
28. Staiger, M. P., Pietak, A. M., Huadmai, J. & Dias, G. Magnesium and its alloys as orthopedic biomaterials: a review. *Biomaterials* **27,** 1728–1734 (2006).
29. Song, G. & Atrens, A. Understanding magnesium corrosion—a framework for improved alloy performance. *Advanced engineering materials* **5,** 837–858 (2003).
30. Song, Y., Shan, D., Chen, R., Zhang, F. & Han, E.-H. Biodegradable behaviors of AZ31 magnesium alloy in simulated body fluid. *Materials Science and Engineering: C* **29,** 1039–1045 (2009).
31. Bose, S., Vahabzadeh, S. & Bandyopadhyay, A. Bone tissue engineering using 3D printing. *Materials today* **16,** 496–504 (2013).
32. Zadpoor, A. A. Additively manufactured porous metallic biomaterials. *Journal of Materials Chemistry B* **7,** 4088–4117 (2019).
33. Putra, N., Mirzaali, M., Apachitei, I., Zhou, J. & Zadpoor, A. Multi-material additive manufacturing technologies for Ti-, Mg-, and Fe-based biomaterials for bone substitution. *Acta Biomaterialia* (2020).
34. Dvorsk, D., Kubásek, J., Vojtěch, D. & Čavojsk, M. Advanced mechanical and corrosion properties of WE43 alloy prepared by powder metallurgy. *Acta Phys. Pol., A* **134,** 748–752 (2018).
35. Gibson, I. *Additive Manufacturing Technologies 3D Printing, Rapid Prototyping, and Direct Digital Manufacturing* 2015.
36. Gonzalez-Gutierrez, J., Cano, S., Schuschnigg, S., Kukla, C., Sapkota, J. & Holzer, C. Additive manufacturing of metallic and ceramic components by the material extrusion of highly-filled polymers: A review and future perspectives. *Materials* **11,** 840 (2018).
37. Arabnejad, S., Johnston, R. B., Pura, J. A., Singh, B., Tanzer, M. & Pasini, D. High-strength porous biomaterials for bone replacement: A strategy to assess the interplay between cell morphology, mechanical properties, bone ingrowth and manufacturing constraints. *Acta biomaterialia* **30,** 345–356 (2016).
38. Lu, Y., Bradshaw, A., Chiu, Y.-L. & Jones, I. The role of $\beta 1$ precipitates in the bio-corrosion performance of Mg–3Zn in simulated body fluid. *Journal of alloys and compounds* **614,** 345–352 (2014).

39. Yan, Y., Cao, H., Kang, Y., Yu, K., Xiao, T., Luo, J., Deng, Y., Fang, H., Xiong, H. & Dai, Y. Effects of Zn concentration and heat treatment on the microstructure, mechanical properties and corrosion behavior of as-extruded Mg-Zn alloys produced by powder metallurgy. *Journal of Alloys and Compounds* **693,** 1277–1289 (2017).
40. Song, Y., Han, E.-H., Shan, D., Yim, C. D. & You, B. S. The role of second phases in the corrosion behavior of Mg–5Zn alloy. *Corrosion Science* **60,** 238–245 (2012).
41. Song, Y., Han, E.-H., Shan, D., Yim, C. D. & You, B. S. The effect of Zn concentration on the corrosion behavior of Mg–xZn alloys. *Corrosion science* **65,** 322–330 (2012).
42. Zeng, R.-c., Zhang, J., Huang, W.-j., Dietzel, W., Kainer, K., Blawert, C. & Wei, K. Review of studies on corrosion of magnesium alloys. *Transactions of Nonferrous Metals Society of China* **16,** s763–s771 (2006).
43. Koç, E., Kannan, M. B., Ünal, M. & Candan, E. Influence of zinc on the microstructure, mechanical properties and in vitro corrosion behavior of magnesium–zinc binary alloys. *Journal of Alloys and Compounds* **648,** 291–296 (2015).
44. Valente, T. Grain boundary effects on the behavior of WE43 magnesium castings in simulated marine environment. *Journal of materials science letters* **20,** 67–69 (2001).
45. Zhang, S., Zhang, X., Zhao, C., Li, J., Song, Y., Xie, C., Tao, H., Zhang, Y., He, Y., Jiang, Y., *et al.* Research on an Mg–Zn alloy as a degradable biomaterial. *Acta biomaterialia* **6,** 626–640 (2010).
46. Geenen, K., Röttger, A. & Theisen, W. Corrosion behavior of 316L austenitic steel processed by selective laser melting, hot-isostatic pressing, and casting. *Materials and Corrosion* **68,** 764–775 (2017).
47. Kong, D., Dong, C., Ni, X. & Li, X. Corrosion of metallic materials fabricated by selective laser melting. *Npj Materials Degradation* **3,** 1–14 (2019).
48. Schweitzer, P. A. *Fundamentals of corrosion* (CRC press, 2010).
49. Wu, H., Zhang, C., Lou, T., Chen, B., Yi, R., Wang, W., Zhang, R., Zuo, M., Xu, H., Han, P., *et al.* Crevice corrosion–A newly observed mechanism of degradation in biomedical magnesium. *Acta biomaterialia* **98,** 152–159 (2019).
50. Jones, D. A. *Principles and prevention of corrosion* **Sirsi) i9780133599930,** 199–201 (1996).
51. Poinern, G. Eddy Jai, Sridevi Brundavanam, and Derek Fawcett." Biomedical magnesium alloys: a review of material properties, surface modifications and potential as a biodegradable orthopaedic implant," *American Journal of Biomedical Engineering* **2,** 218–240 (2012).
52. Nguyen, T., Blanquet, A., Staiger, M., Dias, G. & Woodfield, T. On the role of surface roughness in the corrosion of pure magnesium in vitro. *Journal of Biomedical Materials Research Part B: Applied Biomaterials* **100,** 1310–1318 (2012).
53. Walter, R., Kannan, M. B., He, Y. & Sandham, A. Effect of surface roughness on the in vitro degradation behaviour of a biodegradable magnesium-based alloy. *Applied Surface Science* **279,** 343–348 (2013).
54. Alvarez, R. B., Martin, H. J., Horstemeyer, M., Chandler, M. Q., Williams, N., Wang, P. T. & Ruiz, A. Corrosion relationships as a function of time and surface roughness on a structural AE44 magnesium alloy. *Corrosion Science* **52,** 1635–1648 (2010).
55. Walter, R. & Kannan, M. B. Influence of surface roughness on the corrosion behaviour of magnesium alloy. *Materials & Design* **32,** 2350–2354 (2011).
56. Wang, Z., Guo, W., Li, L., Luk'yanchuk, B., Khan, A., Liu, Z., Chen, Z. & Hong, M. Optical virtual imaging at 50 nm lateral resolution with a white-light nanoscope. *Nature communications* **2,** 1–6 (2011).
57. Carter, C. B. & Williams, D. B. in, 4, 9–16, 39–44, 47, 54–56, 60, 61, 64, 65, 73, 74, 141–169 (Springer, 2009).
58. Zhou, W., Apkarian, R., Wang, Z. L. & Joy, D. in *Scanning microscopy for nanotechnology* 1–40 (Springer, 2006).

59. Kanaya, K. & Okayama, S. Penetration and energy-loss theory of electrons in solid targets. *Journal of Physics D: Applied Physics* **5,** 43 (1972).
60. Kirkland, N., Birbilis, N. & Staiger, M. Assessing the corrosion of biodegradable magnesium implants: a critical review of current methodologies and their limitations. *Acta biomaterialia* **8,** 925–936 (2012).
61. Trasatti, S. & Parsons, R. Interphases in systems of conducting phases (Provisional). *Pure and Applied Chemistry* **55,** 1251–1268 (1983).
62. Rohwerder, M. & Turcu, F. High-resolution Kelvin probe microscopy in corrosion science: scanning Kelvin probe force microscopy (SKPFM) versus classical scanning Kelvin probe (SKP). *Electrochimica Acta* **53,** 290–299 (2007).
63. Yee, S., Oriani, R. & Stratmann, M. Application of a Kelvin microprobe to the corrosion of metals in humid atmospheres. *Journal of the Electrochemical Society* **138,** 55 (1991).
64. Hurley, M., Efaw, C., Davis, P., Croteau, J., Graugnard, E. & Birbilis, N. Volta potentials measured by scanning Kelvin probe force microscopy as relevant to corrosion of magnesium alloys. *Corrosion* **71,** 160–170 (2015).
65. Oernek, C. & Engelberg, D. L. Correlative EBSD and SKPFM characterisation of microstructure development to assist determination of corrosion propensity in grade 2205 duplex stainless steel. *Journal of Materials Science* **51,** 1931–1948 (2016).
66. Souto, R. M., Lamaka, S., González, S., *et al.* Uses of scanning electrochemical microscopy in corrosion research. *"Microscopy: Science, Technology, Applications and Education", Vol. 3 (A. Méndez-Vilas, J. Dıaz, editores). Formatex Research Center, Badajoz (2010), pp. 1769-1780* (2010).
67. Lu, X. & Leng, Y. Theoretical analysis of calcium phosphate precipitation in simulated body fluid. *Biomaterials* **26,** 1097–1108 (2005).
68. Li, X., Liu, X., Wu, S., Yeung, K., Zheng, Y. & Chu, P. K. Design of magnesium alloys with controllable degradation for biomedical implants: From bulk to surface. *Acta biomaterialia* **45,** 2–30 (2016).
69. Oyane, A., Kim, H.-M., Furuya, T., Kokubo, T., Miyazaki, T. & Nakamura, T. Preparation and assessment of revised simulated body fluids. *Journal of Biomedical Materials Research Part A: An Official Journal of The Society for Biomaterials, The Japanese Society for Biomaterials, and The Australian Society for Biomaterials and the Korean Society for Biomaterials* **65,** 188–195 (2003).
70. Dong, J., Tumer, N., Putra, N. E., Zhu, J., Li, Y., Leeflang, S., Taheri, P., Fratila-Apachitei, L., Mol, A. J., Zadpoor, A. A., *et al.* Extrusion-based 3D printed magnesium scaffolds with multifunctional MgF 2 and MgF 2-CaP coatings. *Biomaterials Science* (2021).
71. E112-13, A. *Standard test methods for determining average grain size* 2013.
72. Verhallen, P., Oomen, L., Elsen, A., Kruger, J. & Fortuin, J. The diffusion coefficients of helium, hydrogen, oxygen and nitrogen in water determined from the permeability of a stagnant liquid layer in the quasi-s. *Chemical Engineering Science* **39,** 1535–1541 (1984).
73. Dong, J., Tümer, N., Leeflang, M., Taheri, P., Mol, J., Zadpoor, A. & Zhou, J. Extrusion-based additive manufacturing of Mg-Zn alloy scaffolds. *Under review* (2021).
74. Weller, M., Overton, T., Rourke, J. & Armstrong, F. *Atomic radii* 275 (Oxford, 2010).
75. Örnek, C., Leygraf, C. & Pan, J. On the Volta potential measured by SKPFM–fundamental and practical aspects with relevance to corrosion science. *Corrosion Engineering, Science and Technology* **54,** 185–198 (2019).
76. Zhang, X., Sloof, W., Hovestad, A., Van Westing, E., Terryn, H. & De Wit, J. Characterization of chromate conversion coatings on zinc using XPS and SKPFM. *Surface and Coatings Technology* **197,** 168–176 (2005).
77. Revilla, R. I., Terryn, H. & De Graeve, I. On the use of SKPFM for in situ studies of the repassivation of the native oxide film on aluminium in air. *Electrochemistry Communications* **93,** 162–165 (2018).

78. Kalb, H., Rzany, A. & Hensel, B. Impact of microgalvanic corrosion on the degradation morphology of WE43 and pure magnesium under exposure to simulated body fluid. *Corrosion Science* **57,** 122–130 (2012).
79. Van Gils, S., Mast, P., Stijns, E. & Terryn, H. Colour properties of barrier anodic oxide films on aluminium and titanium studied with total reflectance and spectroscopic ellipsometry. *Surface and Coatings Technology* **185,** 303–310 (2004).
80. Argade, G., Panigrahi, S. & Mishra, R. Effects of grain size on the corrosion resistance of wrought magnesium alloys containing neodymium. *Corrosion Science* **58,** 145–151 (2012).
81. Mouanga, M., Berçot, P. & Rauch, J. Comparison of corrosion behaviour of zinc in NaCl and in NaOH solutions. Part I: Corrosion layer characterization. *Corrosion Science* **52,** 3984–3992 (2010).
82. Roche, V., Koga, G., Matias, T., Kiminami, C., Bolfarini, C., Botta, W., Nogueira, R. & Junior, A. J. Degradation of biodegradable implants: The influence of microstructure and composition of Mg-Zn-Ca alloys. *Journal of Alloys and Compounds* **774,** 168–181 (2019).
83. Mueller, W.-D., Fernandez Lorenzo de Mele, M., Nascimento, M. L. & Zeddies, M. Degradation of magnesium and its alloys: Dependence on the composition of the synthetic biological media. *Journal of Biomedical Materials Research Part A: An Official Journal of The Society for Biomaterials, The Japanese Society for Biomaterials, and The Australian Society for Biomaterials and the Korean Society for Biomaterials* **90,** 487–495 (2009).
84. Liu, C., Xin, Y., Tian, X. & Chu, P. K. Degradation susceptibility of surgical magnesium alloy in artificial biological fluid containing albumin. *Journal of Materials Research* **22,** 1806–1814 (2007).
85. Liu, C., Wang, Y., Zeng, R., Zhang, X., Huang, W. & Chu, P. K. In vitro corrosion degradation behaviour of Mg–Ca alloy in the presence of albumin. *Corrosion Science* **52,** 3341–3347 (2010).

Appendix A

Experimental scanning parameters

Table A.1: SECM scanning parameters used for line scans, approach curves and cylcic voltammetry.

Parameter	**Mode**
Scan axis	X-axis
Conditioning time	10 seconds
Probe current ranging	10 nA/V
Return velocity	100 µm/s
acquisition pre-delay	0.1 seconds
Sample Rate	2000 Hz
Approach curve	
Distance	500-3000 µm
um/point	2-10
Velocity	10-50 µm/s
Maximum bulk	130%
Minimum bulk	88%
Cyclic voltammetry	
Initial potential time	10 seconds
Sweep potential	0.5V
Sweep rate	0.01 V/s
Volts per point	0.1

Table A.2: Scanning parameters used for SKPFM measurements.

Parameter	**Mode**
Lift mode	Enabled
	Dither background
Start height	0.1 µm
Lift height	0.1 µm
Start delay	0.2 seconds
End delay	0.2 seconds
Tip Bias Line Grounded	Enabled
	Forward
Sample Bias Line Grounded	Enabled
	Forward
	Backward
First delay	0.2 seconds
Second delay	0.2 seconds
Sample lines	128-512
Scan rate	0.6 Hz
P	0.5
I	1
D	0
Synchronize to TM frequency	On
AC Bias amplitude	5 V
Lock-in phase	0 V
Lock-in Gain	x20
Lock in filter	2nd order
	2.5 kHz
DC bias Voltage	0 V
SEPM feedback	On
Pi corner Frequency	0.63
Overall grain	∼35/100
Integrator	On
Channels	Height- forward
	Tapping aplitude- backward
	SEPM Error- backward
	SEPM Potential-Backward

Appendix B

X-ray diffractograms

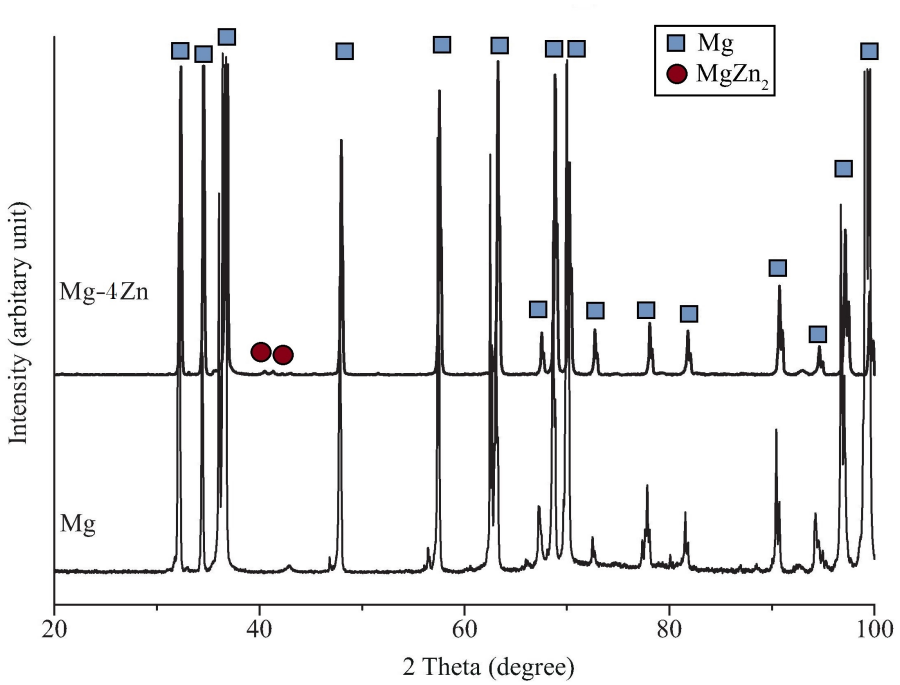

Figure B.1: X-ray diffractogram of an as-sintered alloy [73].

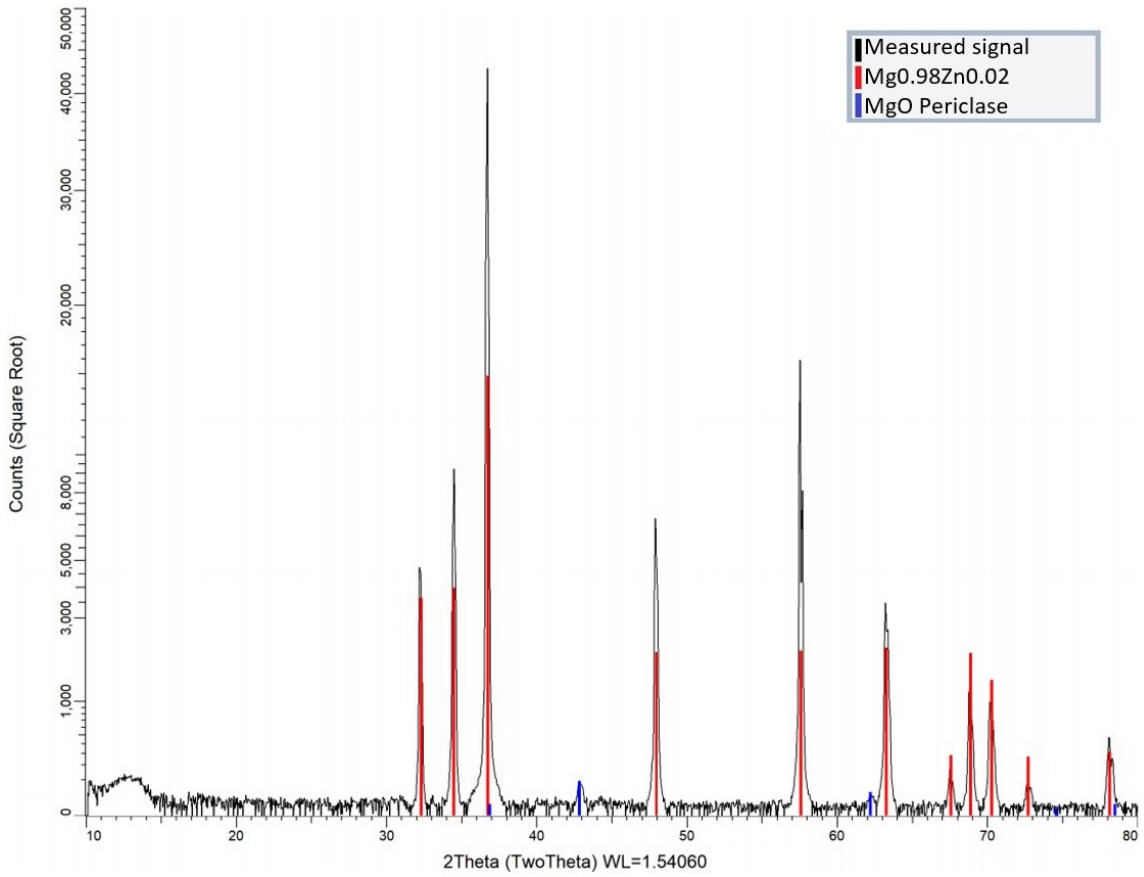

(a)

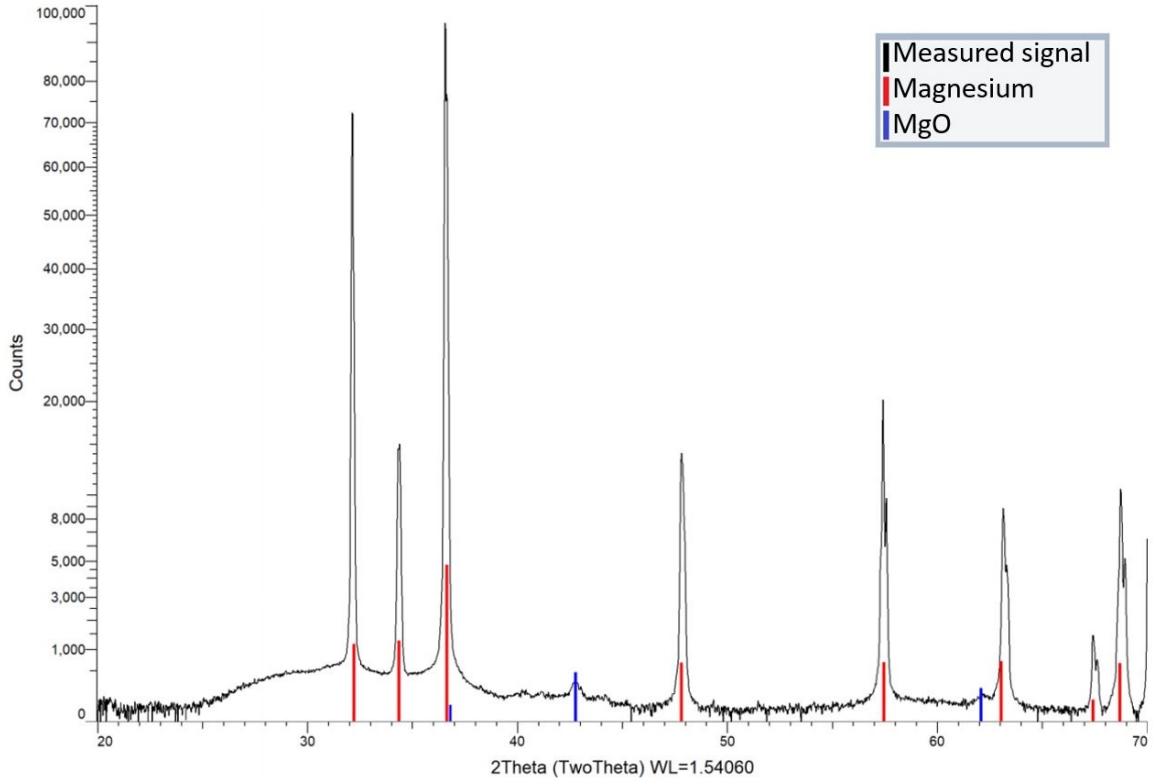

(b)

Figure B.2: X-ray diffractogram of a sanded and polished Mg-4Zn scaffold (a) and after 4.5 hours of immersion in r-SBF (b).